CHALMERS

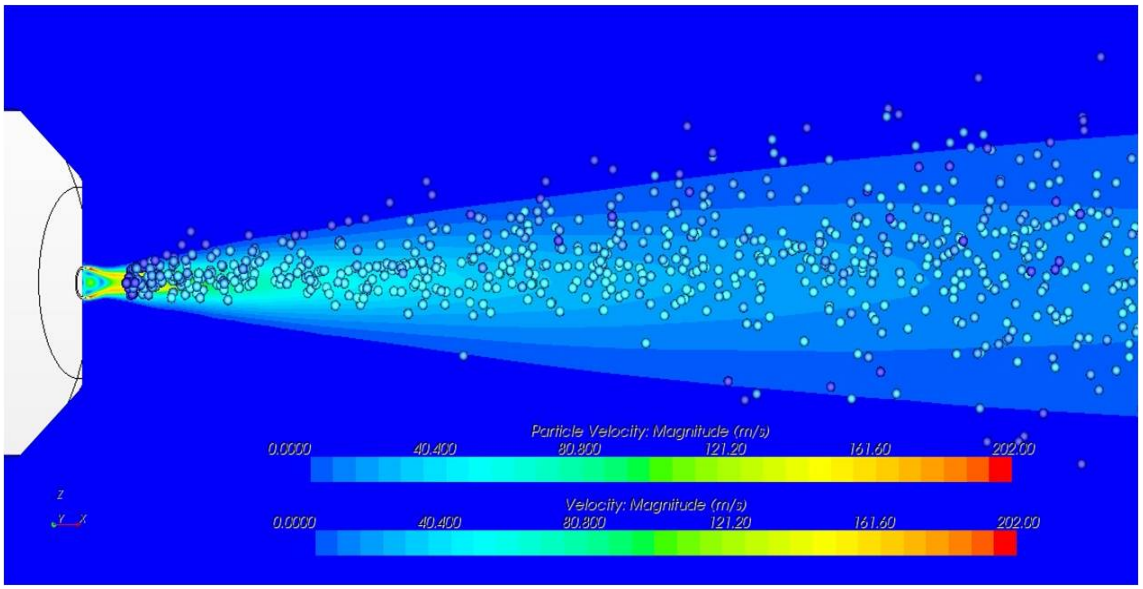

Niklas Löfgren

Air Assisted Urea Spray Modeling

Computational Fluid Dynamics Simulation of Urea-Spray using the Euler-Lagrangian Framwork

Department of Chemical and Biological Engineering
Division of Chemical Reaction Engineering
CHALMERS UNIVERSITY OF TECHNOLOGY
Göteborg Sweden, 2013

MASTER'S THESIS 2013:

Air Assisted Urea Spray Modeling

Master's Thesis

NIKLAS LÖFGREN

Examiner:
Bengt Andersson

Department of Chemical and Biological Engineering
Division of Chemical Reaction Engineering
CHALMERS UNIVERSITY OF TECHNOLOGY
Göteborg, Sweden, 2013

Air Assisted Urea Spray Modeling
Computational Fluid Dynamics Simulation of Urea-Spray using the Euler-Lagrangian Framwork
Master's Thesis
Niklas Löfgren

© NIKLAS LÖFGREN, 2013

Master's Thesis 2013:

Department of Chemical and Biological Engineering,
Division of Chemical Reaction Engineering
Chalmers University of Technology
SE-412 96 Göteborg, Sweden
Phone +46-(0)31-7721000

Cover:
[Particle and air flow close to the spray nozzle, both phases colored by velocity.
For more information see section 4.2]

Printed at Chalmers Reproservice
Göteborg, Sweden 2013

Niklas Löfgren
Master's Thesis
by
Niklas Löfgren
niklof@student.chalmers.se
Department of Chemical and Biological Engineering
Division of Chemical Reaction Engineering
Chalmers University of Technology

Abstract

Decreasing the nitrogen oxide emission is one of the great challenges for the automotive industry today. To include a selective catalytic reaction, SCR, reactor is a popular way to reduce the nitrogen oxide in exhaust gases. For the SCR reactor to work ammonia, often in the form of a urea-water solution spray, needs to be injected into the system. This thesis concerns the simulation of a coaxial air assisted urea spray using computational fluid dynamics. The aim is to propose a model which accurately simulates the urea spray that then can be used in simulations of complete exhaust gas after treatment systems.

The liquid jet breakup, primary atomization, was examined and categorized and the relevance of drop breakup, secondary atomization, investigated. In the simulations the Reynolds Average Navier-Stokes modeling with the Euler-Lagrangian multiphase framework was used. The urea-water solution was injected as drops with a drop size distribution measured 50mm from the spray nozzle. The effect of various particle forces was examined and the two turbulence models Realizable $k - \varepsilon$ and $k - \omega$ SST was compared. The drop velocity, drop size distribution and spray cone angel from the simulations were validated with experimental data, Dahlander and de Benito[1].

The breakup of the liquid jet is likely to produce the final drop size distribution and the subsequent drop breakup seems to be of subordinate importance. The influential particle forces in the simulations are the drag force for deformed particles, the buoyancy force and forces due to turbulence. Of the two turbulence modes the $k - \omega$ SST is the most accurate while the Realizable $k - \varepsilon$ consistently over estimates the drop velocity.

Keywords: CFD, Coaxial air assisted spray, Euler-Lagrangian multiphase, SCR

Acknowledgment

I would like to sincerely thank my Supervisor and Examiner Professor Bengt Andersson for his insightful help and support during this thesis. I am also thankful to Dr. Ronnie Andersson for his ideas and help.

I would also like to especially thank my Supervisor Kerstin Oom for her help, assistance and guidance throughout the thesis.

I also appreciate the kindness and support from the grup Combustion System Analysis and Simulation on Volvo Group Trucks Technology.

Finally, I would like to thank my sister Elise for her support during the thesis, she seems to allways have a minute or two to spare.

Nomenclature

Subscripts

c	Continuous phase
d	Dispersed phase
g	Gas
p	Particle, e.g. drop, droplet, solid particle, bubble
l	Liquid jet

Symbols

B_T	Heat transfer number
C_d	Drag coefficient [-]
CFL	Courant number
$C_{L,S}$	Saffman lift force coefficient [-]
d	Diameter [m]
d_{32}	Sauter mean diameter [m]
E	Aspect ratio [-]
$F_{i,Drag}$	Drag force, see equation 2.14, [N]
$F_{i,Pressure\ and\ Shear}$	Pressure and shear force, see equation 2.15, [N]
$F_{i,Added\ mass}$	Added mass force, see equation 2.16, [N]
$F_{i,History}$	History force, see equation 2.17, [N]
F_{Magnus}	Magnus lift force, see equation 2.18, [N]
$F_{Saffman}$	Saffman lift force, see equation 2.19, [N]
g	Gravity [m/s^2]
h	Energy [J]
h_c	Chemical energy [J]
h_m	Kinetic energy [J]
h_T	Thermal energy [J]
I	Turbulent intensity [-]
I_r	Turbulent relative intensity [-]
k	Turbulent kinetic energy [m^2/s^2]
l	Turbulent length scale [m]
L	Hydraulic diameter [m], length of liquid jet
m	Mass [kg], mass flux ratio
M	Momentum flux ratio
P	Pressure [Pa]
S_P	Source term
S_t	Stokes number
T	Temperature [K, C]
u	Velocity of the continuous phase [m/s]
$\mathbf{u}$	Velocity vector of the continuous phase [m/s]
u'	Fluctuating component of the velocity of the continuous phase [m/s]
u_{rel}	Relative velocity between the dispersed and continuous phase, $u - v$ [m/s]
$-\rho\langle u_i' u_j' \rangle$	Reynolds stress
v	Velocity of the dispersed phase [m/s]
$\mathbf{v}$	Velocity vector of the dispersed phase [m/s]
V	Volume [m^3]

Greek symbols

μ	Dynamic viscosity [Ns/m^2]
ρ	Density [kg/m^3]
σ	Surface tension [N/m]
Φ	Potetial energy [J]

ε	Rate of energy dissipation [m^2/s^3]
ω	specific dissipation rate [1/s]
ν	Viscosity [m^2/s]
ν_t	Turbulent viscosity [m^2/s]
τ_d	Time scale of the dispersed phase
τ_c	Time scale of the continuous phase

Dimensionless numbers

Re	Reynolds number, the ratio of inerta and viscous forces $\frac{\rho_c u L}{\mu_c}$ [-]
Re_{jet}	Jet Reynolds number, the ratio of inertia and viscous forces of the jet $\frac{\rho_l u_l d_{jet}}{\mu_l}$ [-]
Re_p	Particle Reynolds number, the ratio of inertia and viscous forces of the particle $\frac{\rho_c u_{rel} d_p}{\mu_c}$ [-]
We_p	Particle Weber number, the ratio of inertia and surface tension forces $\frac{\rho_c u_{rel}^2 d_p}{\sigma}$ [-]
We_{jet}	Liquid jet Weber number, the ratio of inertia and surface tension forces of the jet $\frac{\rho_g u_{rel}^2 d_l}{\sigma}$ [-]
Oh	Ohnesorge number, the ratio of drop viscous forces to surface tension forces $\frac{\mu_p}{\sqrt{\rho_p d_p \sigma}}$ [-]

Table of Contents

1 Introduction **1**
- 1.1 Purpose . . . 1
- 1.2 Limitations . . . 1
- 1.3 Report outline . . . 2

2 Theory **2**
- 2.1 Flow modeling . . . 2
  - 2.1.1 Turbulence modeling . . . 3
- 2.2 Numerical properties . . . 4
  - 2.2.1 Grid . . . 4
  - 2.2.2 Discretization schemes . . . 4
    - 2.2.2.1 Convectional discretization scheme . . . 4
    - 2.2.2.2 Temporal discretization scheme . . . 5
- 2.3 Convergence criteria . . . 6
- 2.4 Multiphase modeling . . . 6
  - 2.4.1 Fluid particle interaction . . . 6
- 2.5 Breakup . . . 7
  - 2.5.1 Liquid jet breakup- drop and spray formation . . . 8
  - 2.5.2 Drop breakup . . . 9

3 Simulations **11**
- 3.1 Grid generation . . . 11
- 3.2 Single phase simulation . . . 12
  - 3.2.1 Pressure velocity coupling . . . 12
  - 3.2.2 Convectional discretization scheme . . . 13
  - 3.2.3 Boundary conditions . . . 13
- 3.3 Selection of grids and turbulence models . . . 14
- 3.4 Multiphase simulation . . . 14
  - 3.4.1 Phase coupling . . . 14
  - 3.4.2 Drop size distribution . . . 15
  - 3.4.3 Multiphase conditions . . . 16
  - 3.4.4 Particle fluid interaction . . . 17
    - 3.4.4.1 Drag force coefficient . . . 19
      - 3.4.4.1.1 Effects of internal circulation: . . . 19
      - 3.4.4.1.2 Effects of evaporation: . . . 19
      - 3.4.4.1.3 Effects of deformation: . . . 19
    - 3.4.4.2 Saffman lift force coefficient . . . 20
  - 3.4.5 Boundary and initial conditions . . . 21
  - 3.4.6 Discretization scheme . . . 21
  - 3.4.7 Multiphase cases . . . 21
- 3.5 Breakup . . . 22
  - 3.5.1 Jet breakup . . . 22
  - 3.5.2 Drop breakup . . . 23
- 3.6 Convergence . . . 23

4 Results **23**
4.1 Single phase results . . . 23
4.2 Multiphase results . . . 25
4.2.1 Parameter study . . . 25
4.2.1.1 Number of injectors . . . 25
4.2.1.2 Placement of injectors . . . 26
4.2.1.3 Particle forces and interactions . . . 26
4.2.2 Multiphase cases . . . 27
4.2.2.1 Drop axial velocity . . . 27
4.2.2.2 Drop size distribution . . . 29
4.2.2.3 Spray cone angle . . . 30
4.3 Breakup results . . . 31
4.3.1 Jet breakup . . . 31
4.3.2 Drop breakup . . . 32

5 Discussion **34**

6 Conclusion **36**
6.1 Summary . . . 36
6.2 Future work . . . 37

1 Introduction

A great challenge for the automotive industry today is the increasing demand, both by legislation and customers, to reduce emissions from diesel engines. One of the major pollutants in exhaust gas from diesel engines is nitrogen oxides, NO_x, due to their harmful nature to both human health and environment. Nitrogen oxides contribute for instance to smog, acid rain and the destruction of the ozone layer [2, pp. 579-581]. A selective catalytic reaction, SCR, reactor in the exhaust after treatment system has been introduced to reduce nitrogen oxides in the exhaust gas. In the SCR reactor the nitrogen oxides react with ammonia injected into the exhaust gas to create water and gaseous nitrogen as described by the reaction in equation (1.1). Equation (1.1) is unbalanced since NO_X represent both NO and NO_2.

$$NH_3 + NO_X \rightarrow N_2 + H_2O \tag{1.1}$$

The efficiency of the reaction is dependent on how homogeneously the ammonia and exhaust gas are mixed when entering the reactor; hence the ammonia injection system is crucial. One popular way to inject ammonia into the exhaust gas is to inject urea, $NH_2 - CO - NH_2$, and water solution (AdBlue). The urea will decompose to ammonia and isocyanic acid according to equation (1.2a). The isocyanic acid will also convert into ammonia through hydrolyzation in the gas at sufficient temperature or on the SCR catalyst as shown in equation (1.2b), [3].

$$NH_2 - CO - NH_2(s) \rightarrow NH_3(g) + HNCO(g) \tag{1.2a}$$

$$HNCO(g) + H_2O(g) \rightarrow NH_3(g) + CO_2(g) \tag{1.2b}$$

There exist different types of sprays for urea injection, the one investigated in this master thesis, using computational fluid dynamics, CFD, is a coaxial air assisted spray. In this type of spray the AdBlue is injected as a liquid through a circular orifice and high velocity air is injected through an annulus orifice surrounding the AdBlue injection orifice. The high velocity air has the purpose of breaking the AdBlue liquid into small drops.

The spray is a crucial part of the SCR system and therefore important to model accurately as any errors in the spray profile will result in additional errors further down in the system. In order to use simulations to evaluate, improve and/or develop the exhaust gas after treatment system, it is critical that the spray is modeled accurately. To validate the results from the simulations they will be compared to experimental results obtained by Dahlander and de Benito [1].

1.1 Purpose

The purpose of this study is to investigate why and how different CFD models affect the results of simulations of urea spray differently. The aim is to discover a model that accuratley describes the air assisted urea spray. Investigations were performed when the AdBlue was injected as droplets with a given size distribution from the spray nozzle manufacturer and [1]. The effect of liquid jet breakup and drop breakup on the system were also examined. The results will then be validated by experimental data provided in [1].

1.2 Limitations

This thesis will only investigate the spray and not the reactions in the SCR reactor. The simulation setup will be created to resemble the conditions in Dahlander and de Benito experimental study, [1] to enable comparison. This means that the airflow around the spray nozzle will be at room temperature, hence not resemble temperature or flow in an exhaust after treatment system.

Further to match the experimental study, the geometry of the spray will be significantly simplified compared to a real truck exhaust gas after treatment system. The geometry will solely consist of the spray nozzle and a cylindrical control volume. Hence the simulations will be limited and some problems faced in a exhaust gas after treatment system in a real case scenario, e.g. pressure losses over the SCR reactor, will not be included in the simulations.

1.3 Report outline

The report is divided into six chapters where the first contained background and an introduction to the thesis. The second chapter will be a summary of the theory needed to understand the decisions made within the project and the conclusions drawn from the results. The different simulations that were run will be described and the models and methods that were used and why they were chosen will be explained in chapter three. In chapter four and five the results from the simulations will be presented and discussed. In the last chapter the conclusions and a recommended method will be presented and the areas where further studies are needed acknowledged.

2 Theory

In this chapter the theory necessary for this thesis will be presented. The theory concerning the flow modeling will be presented in section 2.1 and the theory about the numerical aspects of the thesis such as discretization schemes and Courant number will be presented in section 2.2. Theory about convergence will be presented in section 2.3 and for the multiphase modeling in section 2.4. Finally the breakup theory will be presented in section 2.5

2.1 Flow modeling

In order to calculate the properties of a flow, mathematical expressions are needed to describe its behavior, i.e. the governing equations. The governing equations are mathematical statements of the conservation laws, i.e. there is no creation or destruction of mass, Newton's second law and the first law of thermodynamics. The governing equations will be stated without derivations, the reader is referred to any textbook in computational fluid dynamics such as [4] or [5] for information about the derivations. The equations for the conservation of mass and the momentum equation, for an incompressible Newtonian flow, are shown in equation (2.1a) and (2.1b).

$$\frac{\partial u_i}{\partial x_i} = 0 \tag{2.1a}$$

$$\frac{\partial u_i}{\partial t} + u_j \frac{\partial u_i}{\partial x_j} = -\frac{1}{\rho}\frac{\partial P}{\partial x_i} + \nu \frac{\partial}{\partial x_j}\left(\frac{\partial u_i}{\partial x_j} + \frac{\partial u_j}{\partial x_i}\right) + g_i \tag{2.1b}$$

Equation (2.1a) is called the continuity equation. The first and second terms in equation (2.1b), also referred to as the Navier-Stokes equation, describes the accumulation and transport by convection of momentum respectively. The third term is a momentum source term due to pressure gradients, the fourth describes the molecular diffusion of momentum and the fifth term is the gravity vector. The energy equation can be expressed as equation (2.2)

$$h = h_m + h_T + h_c + \Phi \tag{2.2}$$

Where h_m is the kinetic energy, h_T is the thermal energy, h_c is the chemical energy and Φ is the potential energy. The transport equation for total energy is presented as equation (2.3).

$$\frac{\partial h}{\partial t} = -\frac{\partial}{\partial x_j}\left[hu_j - k_{eff}\frac{\partial T}{\partial x_i} + \sum_n m_n h_n(-D_n \frac{\partial C_n}{\partial x_j}) - \tau_{kj}u_k\right] + S_h \tag{2.3}$$

In equation (2.3) the first and second terms are accumulation and convection of energy. The third term is the conduction of heat, the fourth is energy due to chemical reactions and the fifth is dissipation of energy. The final term is a general source term, representing for instance cooling of the system. In addition there exist equations for the balancing of species and for each of the different energies in equation (2.3), e.g. the kinetic energy. These equations are not included, instead the reader is referred to [4] or [5] for additional information.

The Navier-Stokes equation can only be solved analytically in very few cases. To solve the equation otherwise the domain has to be discretized into small computational cells, see section 2.2.1. This allows the governing equations, which are partial differential equations, to be integrated over the cell to create algebraic expressions, see section 2.2.2. There are many different approaches to solve the governing equations once the domain is discretized. One approach is to solve the now algebraic governing equations for all entities in every computational cell; referred to as

the Direct Numerical Solution, DNS, method. As no modeling is required in DNS, this is the most exact method but also the most computationally expensive, as it requires a very fine computational grid in order to resolve the smallest scales of the flow. A less computational demanding method is the Large Eddy Simulations, LES, which calculates the larger structures of the flow as in DNS, while the smallest scales are modeled. This makes the LES model less accurate and computational expensive as the smaller scales are not resolved. Another way of filtering the flow is in time domain, which is done in the Reynolds Averaged Navier-Stokes, RANS, method. A RANS simulation is much computationally cheaper and less accurate than LES, because all turbulent structures are modeled.

The DNS and LES models are too computational expensive for most engineering problems and will therefore not be investigated further, instead the RANS method will be described in more detail in section 2.1.1

2.1.1 Turbulence modeling

The basis of the RANS models is to separate the mean and turbulent fluctuating of the flow properties. This procedure is known as the Reynolds decomposition, which for an entity β is given by equation (2.4).

$$\beta_i = \langle B_i \rangle + \beta_i' \tag{2.4}$$

The separation is performed by integrating the entity over time. The time step needs to be long enough to average out all turbulent fluctuations but short enough not to change any eventual transient properties of the mean flow. This integration for entity β is shown in equation (2.5)

$$\langle B_i \rangle = \frac{1}{\Delta t} \int_0^{\Delta t} \beta_i dt \tag{2.5}$$

If the Navier-Stokes equation, (2.1b), is subjected to Reynolds decomposition the result is the so called Reynolds Average Navier-Stokes, RANS, equation shown in (2.6), [6, pp. 34-43]

$$\frac{\partial \langle U_i \rangle}{\partial t} + \langle U_j \rangle \frac{\partial \langle U_i \rangle}{\partial x_j} + \frac{\partial \langle u_i' u_j' \rangle}{\partial x_j} = -\frac{1}{\rho}\frac{\partial \langle P \rangle}{\partial x_i} + \nu \frac{\partial^2 \langle U_i \rangle}{\partial x_j^2} \tag{2.6}$$

The only term in equation (2.6) that differs from the Navier-Stokes equations, (2.1b), is the correlation $\partial \langle u_i' u_j' \rangle / \partial x_j$. This term is called the Reynolds stress tensor, which has six independent unknown quantities, and is a time average momentum transfer rate due to turbulence. This means that for a three dimensional flow there is ten unknown entities, the Reynolds stress tensor, the velocity components and the pressure but only four equations, the Navier-Stokes equations and the mass conservation; hence the system is not closed and has to be modeled. [6, pp. 39-59].

One common way to close the RANS equations is based on the Boussinesq approximation shown in equation (2.7).

$$-\langle u_i' u_j' \rangle = \nu_t \left(\frac{\partial \langle U_i \rangle}{\partial x_j} + \frac{\partial \langle U_j \rangle}{\partial x_i} \right) - \frac{2}{3} k \delta_i j \tag{2.7}$$

Where the scalar ν_t is the turbulent viscosity and the k is the turbulence kinetic energy defined by

$$k = \frac{1}{2}\big(\langle u_1'^2 \rangle + \langle u_2'^2 \rangle + \langle u_3'^2 \rangle\big) = \frac{1}{2}\langle u_i' u_i' \rangle \tag{2.8}$$

The Boussinesq approximation has several limitations. The turbulent structures are assumed isotropic, i.e. independent of direction, which is only valid for turbulent structures on the Kolmogorov scale. Another assumption in the Boussinesq approximation is that turbulent structures behave like molecules, i.e. transfer momentum rapidly, and the local stress and strain are in equilibrium. This implies that models based on the Boussinesq approximation perform badly for highly asymmetric flows, such as swirls, [6, pp. 44, 110 122-123], but the approximation provides the Reynolds stress tensor to be modeled using turbulent viscosity.

Two common models, both based on the Boussinesq approximation are the $k-\varepsilon$ and the $k-\omega$ models. In the $k-\varepsilon$ model the turbulent viscosity is expressed as $\nu_t = C_\mu k^2/\varepsilon$ and in the $k-\omega$ as $\nu_t = k/\omega$. In the expression ε is the energy dissipation rate and ω is the specific dissipation rate, which is to be understood as the inverse of the time scale during which the dissipation occurs, [6, pp. 122-133]. For the equations used to model k, ε and ω the reader is referred to [6]. The expressions for ν_t affect how the models behave and perform in different situations. A major differences is that $k-\omega$ is more accurate in regions with low turbulence. Both k and ε approaches zero with decreasing turbulence. In order for the k-ε model to be accurate the decrease of k and ε must be at a correct

rate, while in the $k-\omega$ model no such restrictions are encountered [5, 118]. Another difference of great interest is in the performance of how well the models predict free shear flows, such as axisymmetric jets, and wakes behind any particles in the flow. In both these situations, according to [6, pp. 136-147] the $k-\omega$ outperforms the $k-\varepsilon$ significantly.

There are several different versions of the two turbulence models, the most relevant to this thesis are the Realizable $k-\varepsilon$ and $k-\omega$ SST models. In the normal $k-\varepsilon$ model the normal stresses, $\langle u_i' u_i' \rangle$, can take negative values for large mean strain rates, see equation (2.7). As the normal stresses by definition are a sum of squares, this value cannot be negative. The Realizable $k-\varepsilon$ model handles this problem changing one of the constants within the model by making it a function, which prevents the normal stresses to be negative. In addition to the normal stress accommodation the Realizable $k-\varepsilon$ modifies the rate of the energy dissipation equation. These adjustmets of the standard $k-\varepsilon$ model makes the Realizable $k-\varepsilon$ model better suited for modeling of axisymmetric jets, [5, 117].

The $k-\omega$ SST model is a hybrid model, where the $k-\omega$ model is used in low turbulence regions and the $k-\varepsilon$ model is used in the regions with fully developed turbulence. In the $k-\omega$ SST model the equations for k and ω, are identical to the $k-\omega$ model but ε is calculated as $\varepsilon = k\omega$, i.e. the ε equation is transformed into a ω equation. The $k-\omega$: SST model is more beneficial than the ordinary $k-\omega$ model as it is more general and gives better values for free shear layers, zero and adverse pressure gradients [4, pp. 90-92].

2.2 Numerical properties

2.2.1 Grid

A necessary step in CFD is to create a computational grid, also called mesh, consisting of computational cells. Creating a computational grid enables the differential governing equations, see section 2.1, to be integrated over the computational cells resulting in linear algebraic expressions. This implies that with sufficient computational power, all systems can be solved. Generally, a denser grid results in more accurate solutions but also increases the computational cost.

Important aspects to consider when generating a mesh are: aspect ratio, ratio between two adjacent cells and skewness. Aspect ratio is the ratio between the long and short side of a cell and should be close to one. A rule of thumb is that the aspect ratio should be below five. This criterion may be relaxed when the cells are aligned with the flow and the stream-wise gradients are small. The size ratio between two adjacent cells should be below two, because very different sizes of adjacent cells will increase the numerical error. Skewness is a measure of how skewed cells are, the maximum skewness should be kept below 0.95, with an average below 0.33, [5, p. 72]

2.2.2 Discretization schemes

Discretization schemes are used to calculate the governing equations presented in section 2.1. For clarification the theory about convectional discretization schemes and for the temporal discretization schemes are presented in separately in section 2.2.2.1 and 2.2.2.2 respectively.

2.2.2.1 Convectional discretization scheme

The value of the various entities are calculated in the center of each cell. To acquire the face value of the cells, which are used to calculate the transport of entities between cells, discretization schemes are used. Hence the choice of discretization scheme must be related to the flow of interest. For a highly convective flow the nodes upstream of the face value should have more influence on the face value than the down-stream nodes. Two such discretization schemes are the first and second order upwind discretization scheme. The ability for the scheme to account for the direction of the flow is called transportiveness, which is desirable as the accuracy of the solution increases. In the first order upwind scheme the face value is taken to be the same as the node value in the neighboring upstream cell. This means than for a entity β, for a flow from left to right in figure 2.1, the first order upwind scheme would give the the β value

$$\beta_r = \beta_i \tag{2.9}$$

The first order upwind scheme is bounded, i.e. the face value can be neither higher nor lower than the node points used to calculate it. This is desirable as enhances stability is obtained [4, pp. 143 -145].

In the second order upwind scheme the face value is determined by the two neighboring upstream cells. If the face value of β should be calculated at face r in figure 2.1, the second order upwind scheme assumes that the gradient

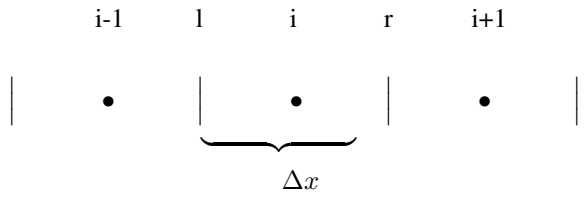

Figure 2.1: The dots represent cell nodes and the vertical lines cell faces. The cell faces for each cell are denoted l for the face left of the node and r for the face right of the node, hence the same cell boundary have different denotations based on the cell considered. The cell boundary for cell i is shown in the figure. The distance between the nodes, and consequently the faces, is assumed to be uniform and denoted Δx.

between face r and node i is equal to the gradient between node i and $i-1$. According to these assumtions the value of β is calculated by:

$$\beta_r = \frac{\beta_i - \beta_{i-1} x_r}{x_i - x_{i-1}} + \beta_i \tag{2.10}$$

The second order upwind scheme is more accurate but also more unstable than the first order upwind scheme. The second order upwind scheme is, in contrast to the first order upwind scheme, unbounded, [5, pp. 49-51].

A major disadvantage with the first order upwind scheme is that high numerical diffusion is generated. This arises because the cell face value is solely determined by the adjacent upstream node, which will overestimate the transport of entities. The overestimation is especially noticeable when the grid is not aligned with the flow, since the value of an entity is constant in a cell.

One way to enhance stability of a simulation is to use part of the old solution, i, together with the new solution, $i+1$, to calculate $i+2$. Using this technique allows smaller steps and reduces the risk of divergence, but more iterations are needed to reach the correct solution. To decide the proportion of new and old solution under-relaxation factors are used. If the under-relaxation factors are chosen to 1 only the new solution is used; if chosen to be 0.5 both solutions are used in equal amounts. If the under-relaxation factors are too low the computational time will be unnecessary long and the risk of false convergence high.

2.2.2.2 Temporal discretization scheme

As for the convective discretization schemes there are several different discretization schemes for the time integration. The forward and backward Euler integration method with uniform time step generate the explicit and the implicit differential scheme respectively [7, pp. 64-69]. In the explicit scheme the solution at time $t + \Delta t$ is solely a function of the solution at present time, t, therefore the solution at time $t + \Delta t$ can be calculated directly. This makes the explicit solver fast and easy to implement, [8, pp. 95-96]. The explicit method is only conditionally bounded; the time step should be chosen so that the Courant number (denoted CFL in equation) (2.11), is below one, i.e. a flow particle should travel a shorter distance during a time step than the length of the cell, [7, pp. 64-69].

The implicit scheme uses backward Euler integration, which means that the solution at time $t + \Delta t$ is a function of both the solution at the present time t and the next time step $t + \Delta t$. The solution at time $t + \Delta t$ is a function of both known and unknown variables therefore the solver has to sub-iterate within each time step to find the correct solution. The implicit solver is unconditionally stable meaning that the solver is, in theory, stable for all choices of time step. However, due to nonlinearities in the governing equations the time step should not be too large. A rule of thumb is that the Courant number, equation (2.11) should initially be five and then increased, [5, p.70] [8, pp. 95-96].

$$CFL = u \frac{\Delta t}{\Delta x} \tag{2.11}$$

2.3 Convergence criteria

There are several indicators of interest used to judge whether a solution has converged or not. In this thesis the primary indicators are residuals, monitors and grid independence. In Starccm+ the residuals in each cell correspond to what degree the discretization equation is satisfied; low correspondence implies large residuals. In order to obtain the residuals for the entire domain the root mean square of the entity is calculated and normalized. When the simulation approaches the correct solution the aberrant of the discretization equation decrease together with the residuals. The normalizing factor in Starccm+ is the largest domain residual of the first five iterations; hence the estimation of the initial solution has a significant impact on the residuals of the system. If the estimated initial solution is close to the true solution the residuals will not decrease as much as if the initial solution guess is poor [9]. This implies that residuals alone are not a sufficient convergence criteria but the residuals can indicate that the solution has convereged. If the residuals decrease to a stable sufficiently low value, and do not increase, this indicates that the solution has converged.

Monitors can be used to check convergence. If for instance the outlet pressure is constant for a number of iterations it is a strong indication that the solution has converged. The final test for convergence is grid independence. Grid indendence means that identical simulations gives the same result with a finer computational grid.

2.4 Multiphase modeling

There are different methods for modeling multiphase flows. Two common approaches with information about individual particles in descending order of accuracy are: the direct numerical solution, DNS, and the Lagrangian-Eulerian framework. In the DNS approach only the interphase between the dispersed and continuous phases is modeled. DNS is very accurate but also very computationally heavy. According to [10, p. 261], DNS computations of a flow with Reynolds numbers in the magnitude of 10 000 can take several weeks. Due to the computational cost DNS is not applicable, with few exceptions, for industrial use.

Within the Lagrangian-Eulerian framework there are two different approaches to handle particles, either as individuals or as bundles. If the particles are treated individually the simulation is more accurate but more computational expensive than if the particles are bundled together in so called parcels. When parcels are used the dynamic properties of the particles, e.g. size and velocity, are identical within the parcel. In the Lagrangian-Eulerian framework each particle-, or parcels interaction with the continuous phase and the interactions between particles or parcels are modeled [10, pp. 235-240] [5, pp. 190-194]. This means that information, such as velocity, position and size of each particle or parcel is known. The forces acting on the particle are presented in section 2.4.1. These forces appear in the governing equations, see section 2.1, as source terms. The Lagrangian-Eulerian framework requires that the computational cell of the continuous phase is larger than the size of the particle. This is because the fluid velocity used to calculate the momentum and mass coupling between the phases need to be the undisturbed velocity, i.e. the velocity of the continuous phase in absence of particles, [5, pp. 190-191].

2.4.1 Fluid particle interaction

Newton's second law states that the rate of momentum change of a particle is equal to the sum of forces acting on the particle, expressed in equation (2.12).

$$F_i = m_p \frac{dv_{p,i}}{dt} \tag{2.12}$$

Where m_p is the particle mass and $v_{p,i}$ is the particle velocity. The force acting on the particle can be divided into body forces, which act on the particle mass, and surface forces, which is caused by pressure and shear stresses acting on the surface of the particle. These forces can then be further bisected, see equation (2.13), [5, pp. 579-581].

$$\begin{aligned} F_i = & F_{i,Drag} + F_{i,Pressure\ and\ Shear} + F_{i,Added\ mass} + F_{i,History} + F_{i,Buoyancy} + F_{i,Lift} + \\ & F_{i,Thermophoretic} + F_{i,Turbulent} + F_{i,Brownian} \end{aligned} \tag{2.13}$$

The forces in (2.13) are briefly described below, for further information the reader is referred to [10, pp. 67-103] and [11]. The drag force $F_{i,Drag}$ act on a particle when the particle and continuous phase have different velocities. The drag force can be expressed accordingly

$$F_{i,Drag} = \frac{1}{2}\rho_c C_D A \mid u_i - v_i \mid (u_i - v_i) \tag{2.14}$$

Where C_D is the drag force coefficient, which is dependent on the flow and particles of interest. The choice of drag force coefficients in this thesis is described in section 3.4.4.1. The pressure and shear force is present if pressure- and shear gradients exist over the particle. The force in an undisturbed flow is then given by

$$F_{i,Pressure\ and\ Shear} = V_p\Big(- \frac{-\partial p}{\partial x_i} + \frac{\partial \tau_{i,k}}{\partial x_k}\Big) \tag{2.15}$$

When a particle is accelerated through a fluid the fluid close to the particle will accelerate at the expense of the particle. This effect is called added mass, and is equivalent to adding mass to the particle. This force can be expressed as

$$F_{i,Added\,mass} = \frac{\rho_c V_p}{2}\frac{D}{Dt}\Big(v_{p,i} - du_i\Big) \tag{2.16}$$

Where D/Dt is the substantial operator. The history force $F_{i,History}$ accounts for the time delay in the development of boundary layers around the particle as the relative velocity between the particle and the continuous phase change over time. The history force can be expressed as

$$F_{i,History} = \frac{3}{2}d_p^2\sqrt{\pi\rho_c\mu_c}\int_0^t \frac{\frac{d}{dt'}(u_{p,i} - v_i)}{\sqrt{t - t'}}dt' \tag{2.17}$$

Where t' is the limit when the time step $\Delta t'$ approaches zero, N is the number of time steps. The time integral needed to solve the history force requires extensive computational time.[5, p. 186].

The buoyancy force, $F_{i,buoyancy}$, is due to the density difference between the particle and the continuous phase. This force is calculated by multiplying the density difference of the phases with the particle volume and gravitational acceleration vector. The lift force can be divided into two parts: the Magnus- and Saffman lift force. Where the Magnus lift force, $F_{i,Magnus}$ is due to rotation of the particle and the Saffman lift force, $F_{i,Saffman}$, is caused by the pressure distribution on the particle due to a velocity gradient. The Magnus lift force can be expressed by the use of a lift coefficient C_M

$$F_{i,Magnus} = \frac{1}{2}C_{Mag}\rho_c A \mid v - u \mid (v - u) \tag{2.18}$$

The Saffman lift force can be calculated by equation (2.19), [12]

$$F_{i,Saffman} = 1.61 C_{L,S}\sqrt{\mu_c\rho_c}d_p^2 \mid u_i - v_i \mid \sqrt{\frac{du}{dy}}sign\left(\frac{du}{dy}\right) \tag{2.19}$$

Where $C_{L,S}$ is the Saffman lift coefficient, which is chosen with respect to the system modeled. The section describing the modeling of $C_{L,S}$ in this thesis is described in section 3.4.4.2

2.5 Breakup

When a liquid jet is injected surrounded by a co-current high speed gaseous annular jet the liquid jet will under certain conditions break into drops. The liquid jet breakup, called primary atomization, and the rules that governs it is described in section 2.5.1. After the jet has broken up there is a possibility that the drops will fragment into smaller droplets. The drop breakup, or secondary atomization, is explained in section 2.5.2. The primary- and secondary atomization determine the final drop size distribution, and to some extent the spray cone angle. To characterize if, where and how the breakup of the jet and drops occur are vital in modeling a spray system.

2.5.1 Liquid jet breakup- drop and spray formation

Disintegration of a liquid jet emanating from a nozzle into ambient motionless gas is fundamentally different from when a coaxial high speed gas stream surrounds the liquid jet. In stagnant gas a liquid jet breaks up due to combinations of initial disturbances of the liquid, aerodynamic forces, surface tension and liquid inertia [13]. In the presence of a high velocity gas stream the liquid jet breakup is, however, mainly caused by the transferal of kinetic energy from the high speed gas to the low speed liquid jet [14].

There are different parameters that affect the breakup of the jet [15], such as the turbulent energy of the liquid jet and the ambient pressure. The most influential parameter that determines the jet breakup is the relative velocity of the gas and liquid. Eddies within and close to the surface of the liquid jet will affect the surface structure as the eddies contain radial velocity components. When the turbulent energy increases so does the energy within the eddies. At sufficiently high turbulent energy the radial velocity component of the eddies will be high enough to overcome the surface tension and create drops even with a relative velocity of zero. The ambient pressure has some influence; higher pressure results in smaller wavelengths of the surface disturbances. The pressure effect is small compared to the turbulent energy of the liquid [15].

When a low velocity liquid jet is surrounded by a co-current high velocity gas, kinetic energy is transferred from the gas to the liquid creating surface disturbances. As the relative velocity between the phases increases the wavelengths of the surface disturbances decrease and ligaments are created [14]. If the relative velocity is increased further the aerodynamic forces overpower the surface tension forces. This causes the ligaments to be accelerated by the air-stream, which decreases the ligament diameter until the ligaments are sheared of the liquid jet and then broken into drops. The drops have an average diameter of ~ 0.4 of the spherical equivalent diameter of the ligament. However, there is a large spread in drop sizes generated by the ligament breakup [16]. The ligaments are quite equally distributed around the liquid jet and the ligament sizes, hence the drop sizes, are strongly dependent on the relative velocity. A larger relative velocity generates smaller ligaments and drops [16]. A schematic figure of the liquid jet breakup is shown in figure 2.2

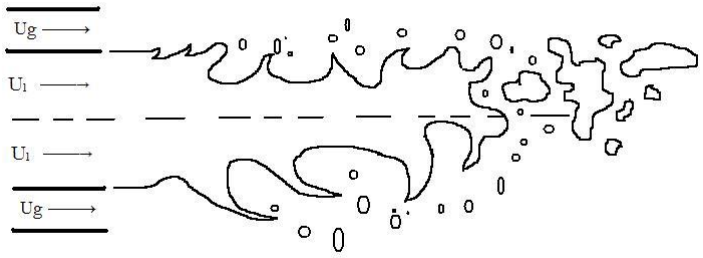

Figure 2.2: A schematic figure of the liquid jet breakup, [14] [17].

Depending on the dominant forces acting on the liquid jet, the breakup of the jet is different. Various breakup regimes can be categorized by the liquid jet Weber number and gas Reynolds number according to table 2.1, [15]. The jet Weber number is defined as $\rho_g u_{rel}^2 d_l/\sigma$ where d_l is the diameter of the liquid jet. Additional parameters influence the breakup regimes, e.g the Reynolds number of the liquid jet and Ohnesorge number, [14]. These parameters will not have a significant effect in the range of liquid jet Weber number treated in this thesis and are omitted.

Table 2.1: Breakup regimes for a round liquid jet as a function of the jet Weber- and Reynolds number.

Breakup regime	Limits
Axisymmetric Rayleigh	$We_{jet} < 15$
Nonaxisymmetric Rayleigh	$15 < We_{jet} < 25$
Membrane breakup	$25 < We_{jet} < 70$
Fiber-type breakup	$70 < We_{jet}$
Superpulsating	$\frac{Re_{jet}}{\sqrt{We_{jet}}} < 100$

In the axisymmetric Rayleigh regime, the breakup is due to hydrodynamic instabilities; the surface energy of the circular jet is not the lowest energy state for the liquid[13]. This means that the liquid stream, due to surface tension, will strive to minimize the surface area. The breakup is initiated by perturbations on the liquid surface, which grows axisymmetrical and after a long enough distance the jet disintegrates into drops with diameter sizes in the same order as the liquid orifice [11, pp. 332-333]. As the relative velocity increases asymmetric disturbances are the primary cause of breakup, this is the Nonaxisymmetric Rayleigh breakup regime.

In the membrane breakup regime waves are formed on the liquid jet surface and are drawn out to sheets as the waves are amplified by the strain imposed by the gas flow. When the aerodynamic forces exerted on the liquid sheets and the Rayleigh instabilities become larger than the surface tension forces the rims of the sheets break up into drops. The liquid sheets are then blown up like bags and fragment into smaller drops [14].

If the Weber number is increased further the jet enters the fiber breakup region. In this region liquid fibers are created and sheared of the liquid jet. These fibers then further fragment to form drops. In this region the surface tension is likely to have a negligible effect on the drop size. Instead the stream-wise eddies in the surrounding gas shear layer may be influential to the drop size. [14] [13].

In the superpulsating region the liquid jet disintegrates rapidly. The liquid jet can be transformed into a liquid sheet, which is then stretched into a membrane with thicker rims. This liquid membrane then bursts into drops of various sizes where the larger drops originate from the thicker rim. The formation and breakup of liquid sheets give the superpulsating breakup region a pulsating behavior where the drops come in chunks rather than being uniformly distributed in time. [15] [13].

2.5.2 Drop breakup

In several situations drops can rupture and create smaller droplets, e.g. collisions with other drops or walls, but in this thesis only particle breakup due to aerodynamic forces are considered. When a drop is subjected to a disruptive flow, the flow tend to deform the drop, while surface tension and viscous forces of the drop strive to resist the deformation. If the disrupting forces, induced by the surrounding flow, are sufficiently large the drop will start to deform. If the aerodynamic forces are larger still the resisting forces are unable to keep the drop intact and the drop will fragment [18] [11, pp. 339-342].

The breakup processes are different for various flows and drops since the breakup is dependent on the interactions and properties of the phases. The different breakup regimes are presented in table 2.2 as a function of the particle Weber number and the breakup processes are shown in figure 2.3 [18]. The particel Weber number is defined as $\rho_c u_{rel}^2 d_p/\sigma$, where d_p is the drop diameter. The limits for the different breakup regimes are not clear, as indicated in table 2.2 and should be understood as indications.

Table 2.2: Drop breakup regimes.

Breakup regime	Limits
Vibrational	$We_p < 11$
Bag	$11 < We_p < 35$
Multimode	$35 < We_p < 80$
Sheet thinning	$80 < We_p < 350$
Catastrophic	$350 < We_p$

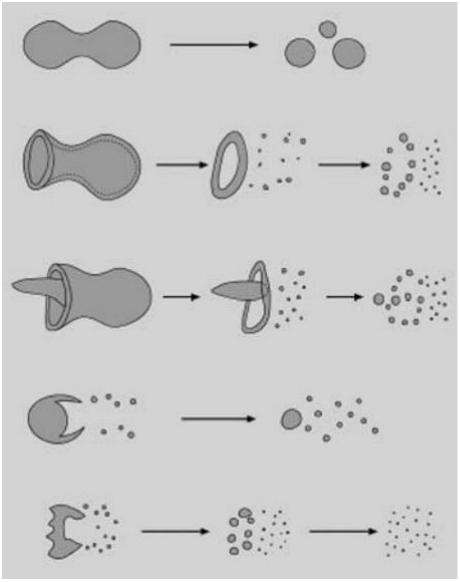

Figure 2.3: Breakup procedure for a Newtonian drop. The breakup regimes are from top to bottom: vibrational, bag, multimode, sheet thinning and catastrophic breakup [18]

If the aerodynamic forces are strong enough to deform the drop but not to cause fragmentation the drop may start to oscillate. The particle oscillations may be stable or unstable depending on the flow conditions. If the oscillations are unstable the drop will eventually break into a few fragments in approximately the size of the original.This is vibrational breakup[18]. Vibrational breakup can, as can be seen in table 2.2, occur at very low Weber number, hence low relative velocity. This breakup regime is not necessarily observed experimentally. The vibrational breakup proceeds slower than the other breakup modes and does not generate small fragment sizes, therefore this breakup regime is often ignored and the bag breakup is instead considered the first breakup regime. The Weber number at which bag breakup initiates is then considered to be the critical Weber number, i.e. where the breakup of drops starts [18].

Bag breakup consists of four stages of which the first is deformation, where the drop flattens from the original spherical shape. In the second stage a pressure difference over the drop causes an indent, which blows up the drop into a bag with a thick rim. The wall of the bag continuously thins out until rupture, which is stage three. The rupture creates a large number of small fragments, with diameters of ~ 4 % of the original drop diameter. In the fourth stage the rim breaks into a small number of larger fragments, with diameters of ~ 30 % of the original drop diameter, containing $\sim$ 60 - 75 % of the original drop volume [11] [18].

A popular theory is that multimode breakup occurs when the effect of the pressure difference over the drop and rapid deformation, which favors sheet thinning of the drop is comparable. In the multimode breakup regime a bag similar to that in the bag breakup regime is formed, the difference is that the center of the drop is blown downstream slower, resulting in a plume, as seen in figure 2.3. First the bag shatters into small droplets followed by the fragmentation of the plume and rim into larger drops. Another possibility for the higher Weber numbers is that the center of the drop is blown downstream slower than the rest of the drop, i.e. a plume is formed but not a bag; the breakup then occurs by continuously stripping small drops from the plume [18].

The first step in sheet thinning is that the particle deforms. Then the inertia of the continuous phase forces the outer edge of the deformed particle to bend towards the flow direction, creating a liquid sheet. The liquid sheet then breaks to ligaments, which subsequently breaks into small drops. The breakup procedure continues until either the drop has ruptured completely or until the drop has accelerated to a speed where the aerodynamic forces become negligible. If the drop has not ruptured completely, extensive amounts of small droplets and a larger drop originating for the original core are formed [18]. In the catastrophic breakup regime the main reason for the breakup is the growth of unstable waves at the leading edge of the drop. The waves grow rapidly and after sufficient time penetrate the drop causing fragmentation. In the early stages of the catastrophic breakup stripping occur at a large portion of the drop surface, opposed to the sheet thinning breakup where liquid is stripped only from the outer edge. After the initial stripping process in the catastrophic breakup mode the drop core is fragmented into large drops

which subsequently are subjected to stripping breakup [18].

3 Simulations

The simulations in this thesis were made in the program Starccm+ and in this chapter the methodology of and reasoning behind the simulations are described. There were a number of cases of interest to simulate, shown in table 3.1.

Table 3.1: The simulated cases in the thesis.

Case	Air flow [liter/min]	AdBlue flow [g/s]
1	10	0.5
2	10	1.5
3	15	0.5
4	15	1.5

The geometry of the injector was supplied by the spray manufacturer. The domain used in the simulations are shown in 3.1. The first step was to create computational grids, see section 3.1. In order to evaluate the quality of the grids single phase simulations were run with different turbulence models, described in section 3.2. These results were then used to choose the grids used throughout the thesis, see section 3.3. In section 3.4 the multiphase simulations are explained, in section 3.5 the breakup of the liquid jet and drops is presented and in section 3.6 the criterias for when a simulation had convergence is explained.

Figure 3.1: The geometry in the simulations, excluding the wall enclosing the system for clarity. The AdBlue injection orifice is 1mm in diameter and the surrounding annulus air injection orifice has an inner diameter of 1.6mm and an outer diameter of 1.9mm. The boundary to the left of the spray is a low velocity inley. The inlet velocity is chosen to be 0.5 m/s to not affect the solution. The boundary to the right is a pressure outlet with no back presure.

3.1 Grid generation

As described in section 2.3 a strong indication that the solution has converged is that two different computational grids give the same results, i.e. the solution is grid independent. To confirm grid independence multiple grids were used in the thesis. Multiphase simulation were planned to be transient using the Eulerian-Lagrangian multiphase framework. This presented contradictory requirements on the grids. The dimensions of the spray nozzle given in figure 3.1 and the airflow in table 3.1 generate a speed of two or three hundred m/s for the exiting high speed gas jet. A very fine cell resolution close to the nozzle were required to capture the nature of the flow. But as described in section 2.4 the Eulerian-Lagrangian framework required the cells to be much larger than the particles and that the

particle volume fraction was small. To follow the recommendations by the Courrant number, see section 2.2.2.2, a coarser grid was preferable as a larger time step could be used. Both of these criteria of a fine and coarse grid could not simultaneously be met, hence a compromise was made.

Grids can be divided into two categories structured and unstructured. The structured grid, in 3D, consists of hexahedral elements. Unstructured grids are built by various bodies, such as prisms, pyramids and polyhedral elements. Structured grids are generally faster, require less memory [5, p. 71] and are more accurate than unstructured grids [19, pp. 250-252]. Some drawbacks with structured grids are that they may be impossible to create for complex geometries, and if the flow is directed towards a corner of the hexahedral element numerical diffusion is generated [5, p74]. The geometry in the simulations were fairly simple therefore a structured grid was possible to generate. A swirl was expected a short distance from the nozzle. This could cause problems as the structured grids would not be aligned with the flow. Some models in Starccm+ needed in the compleat exhaust gas system requier a pollyhedral mesh, why the behaviour of pullyhedral unstructured grids were of interest. Based on these rationales four grids, two structured and two unstructured, were created. The cell sizes were made small at the air jet inlet and were gradually increased with the distance from the spray nozzle. Important features of the grids are given in table 3.2. The main difference between grid one and four were that in grid one the cells were cubes while in grid four cuboidals, with the sides in the streamwise direction three times longer than the other sides. This was done to investigate the possibility to reduce the number of cells and foremost reduce the Courrant number in the later transient simulations by a factor of three. Note that grid three were considerably coarser than the rest, in order to examine if a coarser grid would be possible to use. These four grids were used in the single phase simulations descried in section 3.2.

Table 3.2: Information about the four initial grids used in single phase simulations. S and U represents structured and unstructured grids respectively.

Grid	S/U	Number of cells	Maximum skewness angle [°]	Average skewness angle [°]	Average aspect ratio
1	S	560 000	77.5	1.9	0.98
2	U	500 000	72.3	27.3	0.93
3	U	330 000	68.6	17.9	0.94
4	S	490 000	85.9	7.7	0.91

3.2 Single phase simulation

Work conducted by Oom [20] showed that the use of the turbulence model Realizable $k-\varepsilon$, described in 2.1.1, tended to over predict the particle velocity. To investigate if the simulations was dependent of the turbulence model another turbulence model, $k-\omega$ SST, was used in addition to the Realizable $k-\varepsilon$ model. The $k-\omega$ SST model is described in detail in section 2.1.1. The $k-\omega$ SST was chosen as, according to theory, this model would be more accurate, see section 2.1.1.

3.2.1 Pressure velocity coupling

The pressure and velocity have a coupled interaction in the momentum equation, (2.1b). The momentum equation is, through velocity, coupled with the continuity equation, (2.1a), where no pressure term is present. One way to solve the equations is in an uncoupled iterative manner where an initial guess of the pressure and velocity is used in the momentum equation. Since the initial guess is likely to be incorrect the continuity equation will be unsatisfied. The pressure and velocity are then corrected and the rest of the governing equations are solved. The loop is then repeated until convergence is reached. This iterative method is called the segregated solver [9]. Another way to solve the equations is to solve both the coupled momentum and continuity equation simultaneously in a matrix form, called the coupled solver. The coupled solver is more accurate, better suited for compressible flow and more computational expensive than the segregated solver. The segregated solver can, however, be used for incompressible flows. Since the velocity is as high as 300 m/s the coupled solver might be necessary. To determine the necessity of the coupled solver both solvers were tested.

3.2.2 Convectional discretization scheme

The area of interest was strongly convectional therefore an upwind scheme was chosen, see section 2.2.2. In the beginning of the simulations the first order upwind scheme was used to get an approximate solution, then the second order was used in order to achieve higher accuracy.

3.2.3 Boundary conditions

The most critical boundary condition was the annulus shaped airflow inlet, a badly chosen condition could significantly alter the results. In order to specify the turbulence of the air the turbulent intensity and length scale were used. k and ε or ω could then be calculated from these values. The turbulent intensity and length scale was determined according to the recommendation in [5, p. 138], by equations (3.1).

$$I = 0.16Re^{-\frac{1}{8}} \tag{3.1a}$$

$$l = 0.07L \tag{3.1b}$$

Where I is the turbulent intensity, Re is the Reynolds number, l is the turbulent length scale and L is the hydraulic diameter.

The domain boundary behind the spray nozzle, the leftmost boundary in figure 3.1 henceforth called inlet, was specified as a velocity inlet to prevent any dead zones.The inlet velocity was set low to affect the simulations minimally. This prevented any particle in the multiphase simulations to become stationary in the domain. For the inlet the turbulent intensity and length scale were determined by equations (3.1). But as equations (3.1) are strictly valid for high Reynolds numbers these values were not expected to be good approximations but since the inlet were far from the area of interest the effect on the solution was small. The boundary conditions for the single phase simulations are shown in table 3.3 and 3.4. The results of the single phase simulations are shown in table 4.1.

Table 3.3: Boundary conditions for the single phase simulations for the walls and outlet.

Surface	Boundary type	Condition
AdBlue injection orifice	Wall	No slip
Nozzle walls	Wall	No slip
Boundary Wall	Wall	No slip
Outlet	Pressure outlet	No back pressure

Table 3.4: Boundary conditions for the single phase simulations for the different inlets.

Surface	Boundary type	Condition	Turbulent intensity	Turbulent length scale [m]
Inlet	Velocity inlet	1 m/s	0.049	0.0126
Air injection annulus	Massflow inlet	10 liters/min	0.0615	1.05e-5
Air injection annulus	Massflow inlet	15 liters/min	0.058	1.05e-5

To determine how far into the system the turbulent boundary conditions of the annulus air inlet affect the solution the life time of the large turbulent eddies was multiplied by the average velocity magnitude. This returned an estimate of the distance traveled by large turbulent structures before dying. Large eddies were used in this calculation because they have longer lifetime than smaller eddies hence travels further. See equation (3.2)

$$Distance = \tau_l U = \frac{k}{\varepsilon} U \tag{3.2}$$

Where τ_l is the lifetime of the large turbulent eddies and U is the average velocity magnitude. To estimate k and ε the following relations, from [5, 138] were used

$$k = \frac{3}{2}(UI)^2 \tag{3.3a}$$

$$\varepsilon = C_\mu^{3/4}\frac{k^{3/2}}{l} = 0.09^{3/4}\frac{k^{3/2}}{l} \tag{3.3b}$$

These relations showed that eddies created at the inlet would survive approximately 0.85 mm and 1.1 mm with an air flow of 10 liters/min and 15 liters/min respectively. Calculations showed that the approximate boundary conditions would not affect the solution far into the domain and therefore more exact boundary condition were not necessary.

3.3 Selection of grids and turbulence models

Based on the results from the simulations with the four grids, described in section 3.1, which are presented in section 4.1 the segregated solver was concluded sufficient as the results between the coupled and segregated solver did not deviate significantly. Based on the results in table 4.1 the main grid was chosen to be a structured grid with the stream wise side three times longer than the other. In addition two complementary grids were created: an unstructured, polyhedral grid and a control grid, identical to the main grid except that all cell surface sizes were 10 $\%$ smaller. The control grid were used to investigate if a finer grid would give different results. The unstructured grid was used since some models in the simulations of a complete exhaust gas after treatment system in Starccm+ require a polyhedral grid. Information about the three grids are shown in table 3.5

Table 3.5: Information about the final three grids, S and U represents structured and unstructured grids respectively.

Grid	S/U	Number of cells	Maximum skewness angle [°]	Average skewness angle [°]	Average aspect ratio
Main	S	495 000	72.1	2.2	0.98
Control	S	810 000	64	2.2	0.98
Unstructured	U	510 000	72.3	27.3	0.93

In order to continue investigating the difference between the Realizable $k-\varepsilon$ and $k-\omega$ SST both models were used in the multiphase simulations. Single phase simulations were then made with the three grids and the results are shown in table 4.2.

3.4 Multiphase simulation

3.4.1 Phase coupling

To determine how the phases are coupled the flow can be classified as one-, two- or four way coupled. One way-coupling means that the influence of the particles on the continuous phase and the interactions between the particles are negligible, only the influence of the continuous phase on the particles are important. In this case there is no need to include the particles in the simulation, the particle tracks can be added in the post processing. In two-way coupling the interactions between the phases are no longer negligible and the particles must be included in the simulations but the particle-particle interaction is insignificant. In four-way coupling the particle-particle and particle-fluid interactions are influential [5, pp. 183-184]. The drops were expected to evaporate in the system which implied that the flow was two way mass coupled since mass would be transfered between the phases. The case with the smallest volume fraction was when 0.5g/s AdBlue and 15 liters/min air was injected and the largest volume fraction was encountered for 1.5g/s AdBlue flow and 10 liters/min air flow. With the material properties in table 3.6 this implies that the volume fraction was in the range of $\sim 3*10^{-5}$ and $\sim 1.4*10^{-4}$. These volume fractions gives a average density of the particles and air of $\sim$3.2kg/m^3 and $\sim$6.8kg/m^3 respectively. As the density of air is 1.2kg/m^3 the introduction of particles has an effect on the average density of the flow which implied that the flow was two-way

coupled. To investigate if the flow were four-way coupled a simulation where collision were included was made to determine the importance of particle-particle interactions.

To judge how close the particles folow the motion of the flow, one approach is to consider the ratio between the timescales of the dispersed and continuous phases, i.e. the Stokes number. The Stokes number is defined as the ratio between the particle response time and a relevant timescale for the continuous flow as shown in equation (3.4).

$$St = \frac{\tau_d}{\tau_c} \tag{3.4}$$

If the Stokes number is much less than one, the particle response time is much shorter than a characteristic timescale of the flow. Therefore the particles have plenty of time to adjust to the motion of the continuous flow, i.e. the particles follow the flow pattern of the continuous flow closely. By the same reasoning, if the Stokes number is larger than one the particles will not follow the flow closely and if the Stokes number is much larger than one the motion of the particles are virtually unaffected by the continuous flow pattern [10, pp. 25-26].

The analytical expression for the particle response time, τ_d, is only valid for low Reynolds number flows. Since high Reynolds number flows were examined the analytical expression was invalid. Instead τ_d were estimated as $dv/dt = \frac{1}{\tau_d} u_{rel}$ by evaluating equation (2.13). To estimate τ_d the only particle force taken into account was the drag force, as expected to be dominant. The derivation of τ_d is shown in equation (3.5).

$$m_p \frac{dv}{dt} = \frac{1}{2}\rho_f C_D \frac{d_p^2 \pi}{4} u_{rel} \rightarrow \frac{1}{\tau_d} = \frac{6}{8}\frac{\rho_f}{\rho_p} C_D \frac{u_{rel}}{d_p} \rightarrow \tau_d = \frac{4\rho_p d_p}{3\rho_f C_D u_{rel}} \tag{3.5}$$

Using the mean particle diameters and relative velocities presented in table 3.7, the material properties in table 3.6 and the C_D presented in section 3.4.4 τ_d was estimated to be $\sim 3 * 10^{-4}$. The time scale for the continuous flow was chosen for large turbulent structures, i.e. $\tau_c = k/\varepsilon$. The value,$\tau_c \sim 2 * 10^{-5}$, was obtained from single phase simulations 3 millimeter downstream of the spray nozzle. The estimates of τ_d and τ_c gave a Stokes number of $\sim$15 implying that the particle will not follow the flow closely but will be affected by the motion of the continuous phase.

3.4.2 Drop size distribution

In the simulations the AdBlue was injected as drops with a drop size distribution experimentally determined 50mm from the spray nozzle. In the experimental study [1], used to confirm the simulations, the equipment could only detect particles up to a size of $\sim$ 100 μm. The spray manufacturer's equipment could detect particles of sizes up to 1mm. Consequently the drop sizes provided by the spray manufacturer and the drops size distribution detected in the study [1] did not match. The injection rate of AdBlue was also slightly different, the experimental study [1] had $\sim$ 5 $\%$ lower AdBlue injection rate than the spray manufacturer. The drop size distribution of the drops detected 50mm from the spray nozzle in [1] was calculated for each case and used in the simulations. The different drop size distributions are shown in figure 3.2.

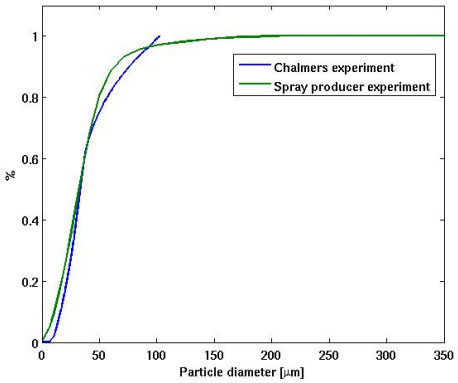

(a) The cumulative drop size when the air is injected 10 liters/min and the AdBlue is injected 0.5 g/s or 0.457g/s.

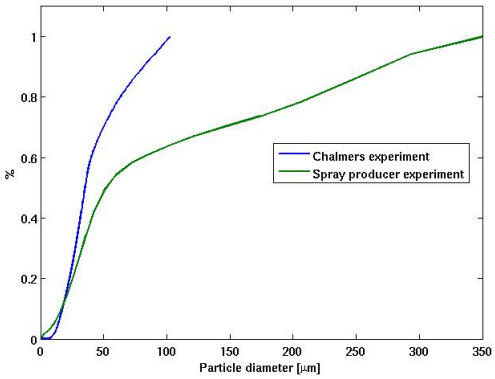

(b) The cumulative drop size when the air is injected 10 liters/min and the AdBlue is injected 1.5 g/s or 1.37g/s.

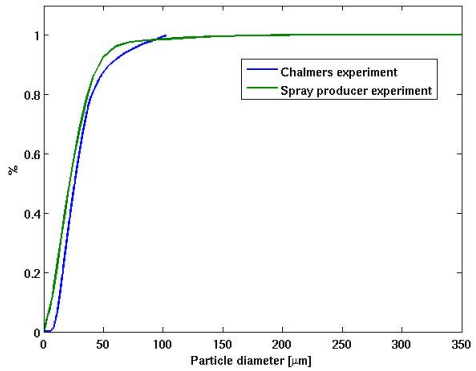

(c) The cumulative drop size when the air is injected 15 liters/min and the AdBlue is injected 0.5 g/s or 0.457g/s

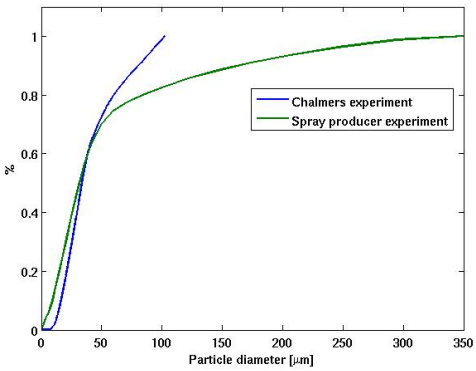

(d) The cumulative drop size when the air is injected 15 liters/min and the AdBlue is injected 1.5 g/s or 1.37g/s

Figure 3.2: The drop size distribution from the nozzle manufacturer and [1].

As can be seen in figure 3.2 the differences between the drop size distributions were in some cases very large. Larger drops than measured were present in the experiment conducted in [1], therefore additional simulations with the drop size provided by the spray producer were made to investigate the effect of the larger drops.

3.4.3 Multiphase conditions

The amount of AdBlue injected was about 0.5g/s or 1.5g/s, which with AdBlue injection orifice diameter of 1mm and AdBlue density in table 3.6, resulted in a AdBlue injection velocity of 0.58m/s or 1.74 m/s respectively. A vortex formed close to the spray nozzle is seen in figure 4.1. If the drops would be injected at the orifice they would be subjected to a counter flow. Since the inertia of the drops was small the drops would be decelerated and subsequently followed the air backwards, collided with the spray nozzle head and then spread out through the entire domain. This behavior was not observed in experiments, [1], where the AdBlue was injected as a liquid jet. To avoid the drops being caught in the vortex, the drops were injected behind the vortex in the simulations. Properties of the multiple multiphase cases are presented in table 3.7 and material properties in table 3.6. The surface tension in 3.6 were for the AdBlue injection condition, i.e. 30^oC. The air jet sourounding the drops were 60^oC at the injection, which means that the temperature of the drops could increase. When the drops started to evaporate the temperature of the drops were expected to decrease. The surface tension is dependent on temperature, within the temperature range 0-60^oC the surface tension of water is in the range 7.6-6.6N/m [21]. If the temperature of the drops increased the surface tension decrease, which increases the Weber number for the drops. If the temperature of the drops decrease the surface tension increase and the Weber number decrease. This implies that the deformation of the particles and, consequently, the drag force increase with increased drop temperature.

Table 3.6: Material properties for the air and AdBlue drops at the injection temperatures 60^{o}C for the air and 30^{o}C for the AdBlue. The surface tension of the AdBlue was taken to be that of water as the surface tension of AdBlue is -to the author's knowledge- unknown. The value of the AdBlue viscosity (at 20^{o}C) and the surface tension were taken from [21] the other values from [22].

Component	Density [kg/m^3]	Surface tension [N/m]	Viscosity [Pa$*$s]
Air	1.05	-	$2*10^{-5}$
AdBlue	1100	0.071	$1.37*10^{-3}$

The relative velocity in table 3.7 was taken as the velocity of the air in the single phase simulations at the location of drop injection at $\sim$ 3mm downstream from the spray nozzle, since the injection velocity if the drops was negligible. The mass mean diameter was used as the average diameter.

Table 3.7: Important features of the multiphase simulations using values from the study conducted by [1] at Chalmers is found in subtable 3.7a and the values provided by the spray manufacturer in subtable 3.7b. The temperature of the air jet and the AdBlue was 333K and 303K respectively in all cases, the surrounding air was set to room temperature to match the experiments in [1].

(a) Chalmers

Air flow [Liters/min]	AdBlue flow [g/s]	u_{rel} [m/s]	d_{mean} [μm]	d_{max} [μm]	Re_p, d_{mean}	Re_p, d_{max}	We_p, d_{mean}	We_p, d_{max}
10	0.458	$\sim$ 100	33	102	200	617	5.5	17
10	1.37	$\sim$ 100	36	102	218	620	6	17
15	0.458	$\sim$ 150	26	102	236	926	9.8	38.3
15	1.37	$\sim$ 150	34	102	309	926	12.8	38.3

(b) Spray manufacturer

Air flow [Liters/min]	AdBlue flow [g/s]	u_{rel} [m/s]	d_{mean} [μm]	d_{max} [μm]	Re_p, d_{mean}	Re_p, d_{max}	We_p, d_{mean}	We_p, d_{max}
10	0.5	$\sim$ 100	40	206	240	1250	6.7	34
10	1.5	$\sim$ 100	114	350	684	2120	19.3	58
15	0.5	$\sim$ 150	28	206	252	1870	10.6	77
15	1.5	$\sim$ 150	64	350	576	3170	24.3	130

3.4.4 Particle fluid interaction

All forces presented in equation (2.13) affect the particles but only forces with a profound effect are desired in the simulations to reduce the computational cost. In the following section the selection of forces is described.

Drag force- was expected to be the single most important force and was included in the simulation, the selection of the drag coefficient is described in section 3.4.4.1.

Forces due to pressure and shear gradients- did not affect the motion of particles if the density ratio between the continuous and dispersed phase was small [10, p. 68-69]. As the spray had a density ratio of $\sim 10^{-3}$ between air and Adblue the pressure and shear force was safely neglected.

Virtual mass force- depended on the density ratio, see equation (2.16), since the density ratio was $\sim 10^{-3}$ the force was neglected.

History force- became less influential with increasing density and size of the particles. A large density difference was a strong indication that the history force could be neglected but not sufficient as other factors such as velocity fluctuations of the continuous phase affected the magnitude of the history force [11, p. 264-265]. Another factor to consider was that the history force would always act in the same direction as the much larger drag force reducing its impact. Based on these arguments and the supporting conclusions that the history force was negligible in similar situations in [3] the history force was excluded from the simulations.

Buoyancy force- was dependent on the density difference between the phases. The density difference was in the order of 1000 therefore expected to be influential and included in the simulation.

Saffman lift force- was in simulations performed on urea sprays in [3] only a few percent of the drag force indicating it could be neglected. The Saffman lift force was always perpendicular to the drag force, i.e the Saffman lift force acted mainly in the radial spray direction. The spray angle in the simulations was important and could potentially be affected by the Saffman lift, hence the force was included in the simulation. The selection of the Saffman lift coefficient is described in section 3.4.4.2

Magnus lift force- was neglected because the Saffman lift force was expected to be one order of magnitude larger and overshadow any effect of the Magnus lift force [3].

Brownian force- was caused by molecular collisions and was only important for submicron particles and was therefore excluded from the simulation.

Thermophoretic force- was important only for tiny particles and in the existence of large temperature gradients. The lack of large temperature gradients, few micro particles and conclusions in [3] the force was exempted.

Turbulence influence- importance was estimated by the relative turbulence intensity, I_r, defined in equation (3.6), [10, p. 80].

$$I_r = \frac{\sqrt{\overline{u'^2}}}{|u_i - v_i|} \tag{3.6}$$

Equation (3.6) can, when the $k-\varepsilon$ and $k-\omega$ turbulence models are used, be rewritten to equation (3.7) since the fluctuation component is $\sqrt{2k/3}$, [6, pp. 44-45].

$$I_r = \sqrt{\frac{2k}{3u_{rel}^2}} \tag{3.7}$$

With increasing turbulent kinetic energy and/or decreasing relative velocity the turbulence intensity increased, see equation (3.7). The turbulence affected the particles in areas of high turbulent kinetic energy, close to the spray nozzle, and/or low relative velocity, further downstream. The high Stokes number of the particles may indicate that the turbulence have a minor effect on the particles as the particles do not follow the flow very closely. There were however a large number of small particles present with low Stokes number for which the forces due to turbulence would be important. Based on this the turbulence influence was included in the simulations. To include turbulent influences Starccm+ used a random walk routine. This was done by adding an eddy velocity fluctuation to the fluid velocity acting on the particle. The eddy velocity fluctuation was assumed to be a normally distributed random number with zero mean and standard deviation given by equation (3.8), [9].

$$u_e = \sqrt{\frac{2k}{3}} \tag{3.8}$$

The eddy velocity fluctuation calculated for a particle remained constant until the interaction with that eddy ended. The particle then entered another eddy and a new random eddy velocity fluctuation was calculated. The interaction time between the particle and the eddy was determined by the smallest of, either the eddy lifetime or, if the relative velocity was non-zero, the time taken for the particle to cross the eddy [9]. This rather simple turbulence

interaction method was computationally cheap but had some shortcomings. Two assumptions built in the random walk routine were: the eddy fluctuating velocity was constant throughout the interaction and the turbulence was isotropic.

The following forces were included in the simulations:

$$F_i = F_{i,Drag} + F_{i,Buoyancy} + F_{i,Saffman\ lift\ force} + F_{i,Turbulent} \tag{3.9}$$

But, as seen in section 4.2.1.3, the Saffman lift force had negligible influence on the results and was later excluded from the simulations.

3.4.4.1 Drag force coefficient

A common drag coefficient correlation, acquired from [11, p. 112], is presented in equation (3.10).

$$C_{D,\ solid\ sphere} = \frac{24}{Re_p}\Big(1 + 0.2Re_p^{0.63}\Big) \tag{3.10}$$

This correlation is valid for a perfect solid sphere in the region $20 \leq \ Re_p \ \leq 260$. To capture the behavior of a liquid drop some alterations to the C_D correlation was considered. Three aspects were examined: deformation, internal circulation, and evaporation. As the drops were accelerated by the fluid the particle Reynolds number decreased and could fall below the limit of 20 for the correlation in equation (3.10). To accurately describe the drag force of the particles with low relative velocity a second correlation shown in equation (3.11), also from [11, p. 112], was used for the particles with Reynolds numbers below 20.

$$C_{D,\ low\ particle\ Reynolds} = \frac{24}{Re_p}\Big(1 + 0.13Re_p^{0.82-log_{10}(Re_p)}\Big) \tag{3.11}$$

3.4.4.1.1 Effects of internal circulation: Internal circulation is created by the viscous shear stress exerted by the continuous phase upon the drop interface, i.e. the continuous phase forces the fluid close to the drop surface to move in a co-current motion to then recirculate back into the middle of the particle. The internal circulation would decrease the relative velocity between the phases and consequently the drag force. As viscous shear stress was the source of internal circulation the viscosity of the different phases were important. If the viscosity of the particle was much larger than the continuous phase the internal circulation would be small and vice versa. Internal circulation could under some circumstances reduce the drag coefficient of a fluid particle to one third of the drag coefficient of an equivalent solid sphere [3]. According to [23] the correlation between the drag force for a fluid particle with internal circulation and a solid spherical particle can be described as equation (3.12).

$$F_{Drag,\ internal\ circulation} = \left(\frac{2 + 3\frac{\mu_d}{\mu_c}}{3 + 3\frac{\mu_d}{\mu_c}}\right)\Big(1 - 0.03\frac{\mu_c}{\mu_d}Re_p^{0.65}\Big) \times F_{Drag,\ solid\ sphere} \tag{3.12}$$

Equation (3.12) was evaluated with the values in table 3.6 and 3.7 for the drops at the injection point. The largest deviation between a solid sphere and liquid drop was below 5 $\%$ in all cases calculated with the mean diameter. For the most extreme case the deviation using the maximum diameters was ~ 9 $\%$, implying the internal circulation would be important. The particles were expected to accelerate fast, i.e. the particle Reynolds number would decrease over a short distance, resulting in a negligible effect of internal circulation even for the largest particles. The viscosity ratio used in (3.12) depended on the temperature variation and the amount of water in the AdBlue drops. Extensive changes in the temperature of the phases and water concentration in the drops alter the viscosity ratio but neither of these scenarios were expected due to low temperatures in the domain. The effect of the internal circulation on the drag force was therefore omitted as internal circulation were insignificant a short distance from the nozzle.

3.4.4.1.2 Effects of evaporation: Low temperatures in the system implied slow evaporation rates, also shown by simulation made by Oom [20], therefor the evaporation effect on the drag force was not considered.

3.4.4.1.3 Effects of deformation: If a relative velocity existed between a drop and the continuous phase the drop would be subjected to an inertial force, which would attempt to deform the drop, while surface tension and viscous forces would strive to maintain a spherical shape. Deformation of the drops would change the projected area and consequently increase the drag force up to ~ 3 times the equivalent undeformed drop [11]. An adjustment in the

drag coefficient for deformation, suggested in [23], expressed in terms of the Weber and particle Reynolds number is shown in equation (3.13).

$$C_{D,\,deformed\,sphere} = C_{D,\,solid\,sphere}\left(1 + 0.06Re_p^{-0.12}We_p^{1.4}\right) \tag{3.13}$$

This correlation is valid in the range $20 \leq\ Re_p\ \leq 200$. The deformation of a drop expressed by aspect ratio, E, can be estimated by a function using the particle Weber number as in equation (3.14), [24]

$$E = 1 - 0.7\tanh(0.07We_p) \tag{3.14}$$

Equation (3.14) is valid for $We_p < We_{crit}$. The aspect ratio evaluated for a drop at the injection point, see table 3.7, was ~ 0.6, which implied that the deformation effect was likely to be crucial. The drag coefficient for the higher particle Reynolds number, equation (3.10), was therefore corrected for particle deformation using equation (3.13). The aspect ratio for a drop at the upper limit of the lower particle Reynolds number drag coefficient, equation (3.11), i.e. $Re_p = 20$, became ~ 0.997. This implied that the deformation would be unimportant for the lower particle Reynolds number drag force coefficient. The final drag force coefficients are presented in equation (3.15)

$$C_D = \frac{24}{Re_p}\left(1 + 0.13Re_p^{0.82-log_{10}(Re_p)}\right) \quad Re_p \leq 20 \tag{3.15a}$$

$$C_D = \frac{24}{Re_p}\left(1 + 0.2Re_p^{0.63}\right)\left(1 + 0.06Re_p^{-0.12}We_p^{1.4}\right) \quad 20 < Re_p \tag{3.15b}$$

An alternative approach to account for drop deformation was the Taylor Analogy Breakup, TAB, model in Starccm+. In order to calculate the drop distortion the TAB model used an analogy between distortion of particles and a damped spring system. The driving force for the distortion was the interaction between the continuous phase and the particle. The restoring force was the surface tension and inertial damping [25]. The distortion y was calculated by equation (3.16). When y equaled zero the particle was considered a sphere and when y equaled one the drop was disk shaped [25].

$$\ddot{y} + C_d\frac{\mu_p}{\rho_p r^2}\dot{y} = \frac{C_F\rho_g u_{rel}^2}{C_b\rho_d r^2} \tag{3.16}$$

The TAB distortion model interpolated between the drag coefficient of a sphere and a disk using y. For additional information about the TAB model the reader is referred to [25] and [26].

The disadvantages with the TAB model were that phenomenas such as evaporation and internal circulation were difficult to add to the drag coefficient should they be important. The correlation for the drag force coefficient presented in equation (3.15) was used instead of the TAB model because of the possibility to easily adjust for physical phenomenas with potential influences. However, to compare the results from the two approaches the TAB model was used once. The drag coefficients were limited to particle Reynolds numbers below 200. In table 3.7 considerably higher particle Reynolds number are listed but the drops were expected to accelerate fast, violating the particle Reynolds number criterion only a short distance. The extent of the violation was later established from the simulations.

3.4.4.2 Saffman lift force coefficient

The Saffman lift force coefficients proposed in [12] and [27] are shown in equation (3.17).

$$C_{L,S} = (1 - 0.3314\sqrt{\psi})exp\left(\frac{-Re_p}{10}\right) + 0.3314\sqrt{\psi} \quad Re_p \leq 40 \tag{3.17a}$$

$$C_{L,S} = 0.0524\sqrt{\psi Re_p} \qquad Re_p \geq 40 \tag{3.17b}$$

The correlations were developed based on numerical results and are valid for spherical particles with particle Reynolds number up to 100 [12] and ψ is given by

$$\psi = \frac{d_p}{2u_{rel}}\left|\frac{\partial u}{\partial n}\right| \tag{3.17c}$$

Where $\partial u/\partial n$ is the velocity derivative in the direction normal to the particle movement, i.e. approximately in radial direction of the spray. Once again the particle Reynolds numbers in the simulations were above the upper limit for the Saffman lift force coefficient correlation, but the Reynolds numbers were expected to decrease rapidly as the particles were accelerated by the flow.

3.4.5 Boundary and initial conditions

The boundary conditions for the flow were identical to the single phase simulations described in section 3.2.3 with the addition that if a drop hit any wall the drop escaped the domain. The drops were injected through point injectors with a temperature of 30^{o}C and axial velocities of 0.58m/s and 1.74 m/s for AdBlue injection rates of 0.5g/s and 1.5g/s respectively. To inject the drops at one point poorly described the system, since the AdBlue injection orifice had a diameter of 1mm. Rather a number of points spread out within the high speed gas jet were used. The number of injection points, the distance from the nozzle and the area of the radial spread of the injection points were varied to investigate the effects on the results. The number of parcels injected were $\sim$ 500 000 parcels per second. This number was a reasonable to use as in a complete exhaust gas after treatment system simulation a larger number would have been too computational heavy. For a summary of the cases tested see table 3.8. To save computational time the solutions from the single phase simulations were used as initial conditions for the multiphase simulations.

3.4.6 Discretization scheme

In the multiphase simulations the second order upwind scheme was used throughout the simulations due to the higher accuracy than the first order upwind scheme, see section 2.2.2.1. The chosen temporal discretization scheme was the implicit method as it was unconditionally bounded, see section 2.2.2.2. The unconditionally bounded discretization scheme enabled a larger time step than otherwise would have been possible.

The time step for the spray was chosen to $1*10^{-4}$ seconds, which was too large to meet the Courant criteria, see equation (2.11). Given the size of the cells close to the high velocity air inlet the Courant numbers were $\sim$ 200, $\sim$ 222, and $\sim$ 400 for the main, control and unstructured grid respectively for an air flow of 15 liters/min. With an air flow of 10 liters/min the Courant numbers were two thirds of the 15 liters/min values. The Courant numbers decreased rapidly as the air speed decreased and the cell size increase. For the air flow 15 liters/min, 10mm downstream of the spray nozzle the Courant number was below 15 for all grids.

3.4.7 Multiphase cases

To determine how many injectors needed each of the air and AdBlue injection speeds presented in table 3.7a were simulated with 9, 13, 17 and 25 injectors with the main grid. Drop size distributions from the Chalmers experiment were used to enable data comparison. In the simulations 500 000 parcels/s were used, 50 per time step, these had to be spread out on the injectors. The drop size distribution from the spray manufacturer were presented in a table with around 30 drop diameters and the mass percent for each interval was provided. Intervals with large mass percentiles were split until 50 intervals with $\sim 2\%$ of the mass in each interval was obtained. The 50 drop sizes were then spread out on the different injectors. This was done to ensure an even mix of drop sizes over the injection area. The size distribution from the experimental study [1] was created by calculating 50 intervals of drop sizes from the detected particles 50mm from the spray nozzle. The simulations were made according to the base case in table 3.8

To save computational time the effect of various parameters, such as adding the Saffman lift force, were only tested for the case with air flow 15 liters/min and AdBlue flow 1.46 g/s. The simulations in table 3.8 were compared with the base case to evaluate the parameters' effect on the solution. The different parameters tested are presented in table 3.8 and the results of the simulations in section 4.2.

Table 3.8: The various simulations used to evaluate the effect of different parameters on the results. Detailed drag law implied that the coefficient presented in equation (3.15) was used. Spherical drag law used the drag force coefficient without deformation, i.e. equation (3.10) and (3.11). $d_{injection}$ was the diameter of the injection area and Δz was the axial distance from the spray nozzle where the drops were injected. All cases had the air flow 15 liters/min, AdBlue flow 1.46 g/s and drop size distribution from Chalmers. The grid used in the simulations was the main grid and the turbulence model was the $k-\omega$ SST model.

Case	Particle forces	$d_{injection}$ [mm]	Δ z [mm]
Base case	Detailed drag law, buoyancy force, turbulent dispersion	1.4	3
Case 1	Base case	1	0
Case 2	Base case	1	3
Case 3	Base case	1.6	3
Case 4	Base case	2	3
Case 5	Base case	2.4	3
Case 6	Base case + Saffman lift force	1.4	3
Case 7	Base case + particle collisions	1.4	3
Case 8	TAB drag law, buoyancy force, turbulent dispersion	1.4	3
Case 9	Spherical drag force, buoyancy force, turbulent dispersion	1.4	3

The cases in 3.7a were simulated with 25 injectors with all three grids and both the Realizable $k-\varepsilon$ and $k-\omega$ SST turbulence models under base case conditions. The results of these simulations are shown in section 4.2. To determine if the results were affected by including the larger drops detected by the spray manufacturer the cases in table 3.7b were simulated with 25 injectors with the main grid and the same settings as the base case in 3.8. The results from these simulations are shown together with results from the breakup simulations in section 4.3.

3.5 Breakup

3.5.1 Jet breakup

Jet breakup would have been extremely computationally expensive to simulate because a very fine grid, more advanced turbulence- and multiphase models would have been needed. However, some aspects of the jet breakup were determined without simulations. The jet Weber numbers We_{jet} were, using the material properties in table 3.6, ranging from $590 < We_{jet} < 1330$ for air and AdBlue injection rates. The Reynolds numbers of the liquid jets using the diameter of the jet as characteristic length, were in the range of $460 < Re_{jet} < 1400$ for the different AdBlue injection velocities. Using the jet Weber and Reynolds numbers the interval $10 < Re_{jet}/\sqrt{We_{jet}} < 60$ was calculated. The breakup regions in table 2.1 showed that all cases treated in this thesis were in the superpulsating breakup regime.

The primary parameter determining the length of the liquid jet before being disintegrated was the momentum flux ratio, defined: $M = \rho_g u_g^2/\rho_l v_l^2$. The length of the liquid jet decreased with increasing momentum flux ratio, [14]. If the momentum flux ratio was above ~ 50 a vortex was formed downstream the liquid core. The momentum flux ratio was for the cases with AdBlue injection rate of 0.5g/s significantly above the critical value of 50. The liquid jet in the cases with AdBlue injection rate of 0.5g/s was curtailed by the recirculating motion of the gas downstream. The lengths of the liquid jets were approximated with equation (3.18), [14].

$$L = d_l \frac{6}{\sqrt{M}} \left| 1 - \frac{v_l}{u_g} \right|^{-1} \tag{3.18}$$

The Sauter mean diameter, d_{32}, of the drops created in the liquid jet breakup was estimated by equation (3.19), [28].

$$d_{32} = \frac{0.0021(\rho_l \nu_g)^{1/4}\sqrt{\sigma}}{\rho_g^{3/4}(v_g(1+\sqrt{\frac{\rho_g}{\rho_l}} - v_l)u_g^{1/4}} \tag{3.19}$$

Equations (3.18) and (3.19) were evaluated for the multiple cases and the results are presented in section 4.3

3.5.2 Drop breakup

The drop Weber numbers in table 3.7 implied that the larger drops would shatter according to bag, multimode or sheet-thinning breakup. The high velocity air jet decelerated fast due to stagnant surrounding air and energy needed to accelerate the drops. This implied that the relative velocity decreased rapidly with increasing distance from the spray nozzle. The relative velocity of 46m/s was required for the largest drops, $d = 350\mu m$, to enter the bag breakup regime, i.e. $11 < We_p$. The breakup was therefor expected to take place within the first few millimeters from the spray nozzle. To control if breakup affected the results of the simulations the cases in table 3.7b were simulated using the main grid, $k-\omega$ SST turbulence model and the TAB breakup model. The TAB model broke a drop when y, see section 3.4.4.1, was above or equal to one. The critical Weber number in the TAB model was specified to 11. For additional information about the TAB model the reader is referred to [25] and [26]. The results from the simulations are presented in section 4.3

Potentially, turbulence of the gas jet could rapture the drops. Particles larger than the Kolmogorov length scale would be subjected to an irregular flow field which could fragment the drops [18]. The Kolmogorov length scale, given by $\eta = (\nu_g^3/\varepsilon)^{1/4}$, was assessed for the two air flows using ε values from the single phase simulations 3mm downstream the spray nozzle and properties from table 3.6. For the air flow 10liters/min and 15liters/min the Kolmogorov length scale was $\sim 5\mu$m and $\sim 3\mu$m respectively. This implied that the vast majority of the drops were subjected to an irregular flow field due to turbulence. An estimate of the axial distance from the spray nozzle to the end of the region where turbulent breakup could occur from [14], is shown in (3.20)

$$x_{crit} \simeq u_g^{-4/5}\left(\frac{1}{d_g(1+m)}\right)^{-3/5}\left(\frac{\sigma}{\rho_g}\right)^{2/5} \tag{3.20}$$

Where m in equation (3.20) was defined as

$$m = \frac{\rho_l v_l A_l}{\rho_g u_g A_g},$$

and the areas, A, were the cross-sectional area of the liquid- and gas nozzle. Equation (3.20) was evaluated for the various cases and the results are shown in section 4.3.

3.6 Convergence

To ensure the simulations had converged different residuals and various monitors were used. The simulation monitors were the mass flow in and out from the domain, the velocity 10mm, 30mm, 50mm and 70mm from the spray nozzle, the temperature and pressure at the outlet. When these monitors showed a constant and realistic value and the residuals were stable the solution was considered converged. The results from the main and control grid were compared.

4 Results

4.1 Single phase results

Two entities, maximum velocity and spreading rate, are used to compare the solutions for the various single phase simulations at 30mm and 50mm from the spray nozzle. The spreading rate is defined as the radial distance where the velocity is half of the velocity in the center of the jet. The results for the first four grids described in section 3.1 are shown in table 4.1. Grid one and four are structured grids with the main difference that the cells in grid four are three

times longer in the stream wise direction. Grid two and three are unstructured, polyhedral grids where grid three is considerably coarser than the other grids. Only the results for the segregated solver are shown as the results from the coupled and segregated solver deviate less than 2%, with the exception of grid three. The results in table 4.1 for grid three is inconsistent with the other grids. Grid three is therefore concluded to be too coarse and omitted from further discussion. Trends are detected in grids one, two and four. The $k-\omega$ SST turbulence model consistently gives lower maximum velocities and a larger spreading rate than the Realizable $k-\varepsilon$ mode. The difference between the two turbulence models and three grids decrease with increasing distance from the spray nozzle.

Table 4.1: Results from the single phase simulations with the first four grids, described in section 3.2. The results shown are the maximum velocity, in m/s, and the spreading rate in millimeters at 30mm and 50 mm from the spray nozzle. For all these cases the air flow is 15 liters/min.

Distance	30 mm				50 mm			
	u_{max}		$Spreading\ rate$		u_{max}		$Spreading\ rate$	
	$k-\varepsilon$	$k-\omega$	$k-\varepsilon$	$k-\omega$	$k-\varepsilon$	$k-\omega$	$k-\varepsilon$	$k-\omega$
Grid 1	53.5	50.5	3.1	3.4	33	29	5.1	5.7
Grid 2	55.5	52	2.9	3.3	33.5	30	5	5.6
Grid 3	90	57	1.7	2.8	65	33	2.4	4.9
Grid 4	56	53	3	3.3	33	31	5	5.7

The results from the single phase simulations with the main, control and unstructured grids are shown in a similar manner in table 4.2. The same trends as in table 4.1 are observed, i.e. Realizable $k-\varepsilon$ turbulence model gives higher velocities and lower spreading rate than the $k-\omega$ SST turbulence model. In addition the largest observed difference between the three grids is below 5%.

Table 4.2: Results from the single phase simulations with the main, control and unstructured grids described in section 3.2. The results shown are the maximum velocity in m/s and the spreading rate in millimeters at 30mm and 50 mm from the spray nozzle for airflow of 10 liters/min and 15 liters/min.

Distance	30 mm				50 mm			
	u_{max}		$Spreading\ rate$		u_{max}		$Spreading\ rate$	
	$k-\varepsilon$	$k-\omega$	$k-\varepsilon$	$k-\omega$	$k-\varepsilon$	$k-\omega$	$k-\varepsilon$	$k-\omega$
Shows the results for 10 liters/min air flow								
Main grid	39	36.5	3.1	3.3	23.5	21	5.2	5.7
Control grid	38.5	36.5	3	3.3	24	21.5	5.1	5.8
Unstructured grid	37.5	35	3.2	3.3	22	21	5.3	5.7
Shows the results for 15 liters/min air flow								
Main grid	57.5	53.5	3	3.3	33.5	30.5	5.1	5.7
Control grid	58.5	53	3	3.3	35	30.5	5.1	5.8
Unstructured grid	56	52	3	3.3	33	30	5	5.7

The air jet flow pattern is shown in figure 4.1, where the left hand side shows the velocity magnitude on a plane cutting the center of the spray nozzle and the right hand side displays the vortex close to the nozzle. The figure shows only one grid and turbulence model, the main grid and the $k-\omega$ SST model. The other cases give similar flow patters. The distance from the nozzle to the end of the vortices is below 2 mm for both airflows and all grids, where the vortex is slightly larger for the higher airflow.

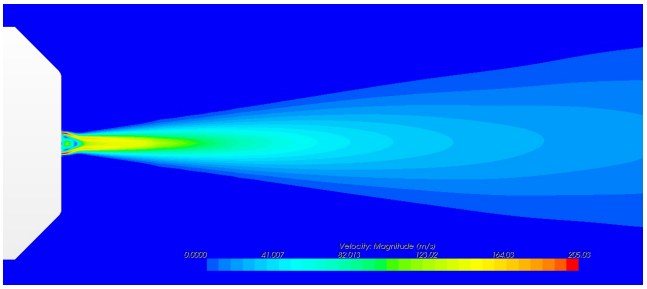

(a) The velocity magnitude profile for the air jet for air flow 10 liters/min.

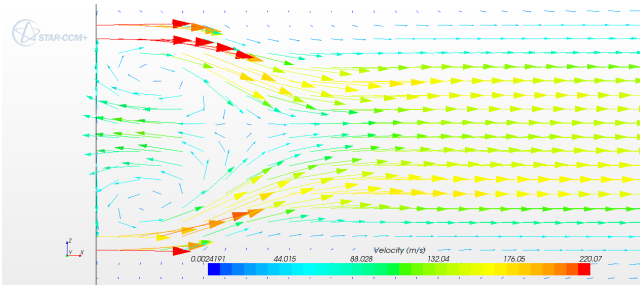

(b) The vortex that forms close to the nozzle inlet for air flow 10 liters/min.

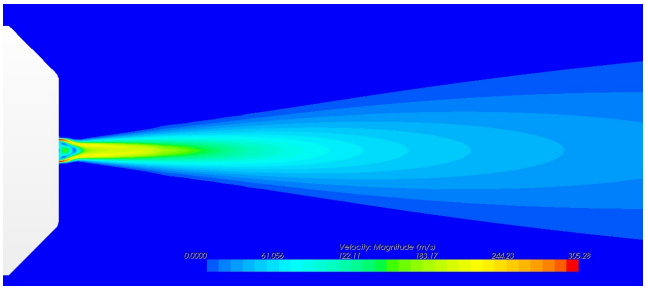

(c) The velocity magnitude profile for the air jet for air flow 15 liters/min.

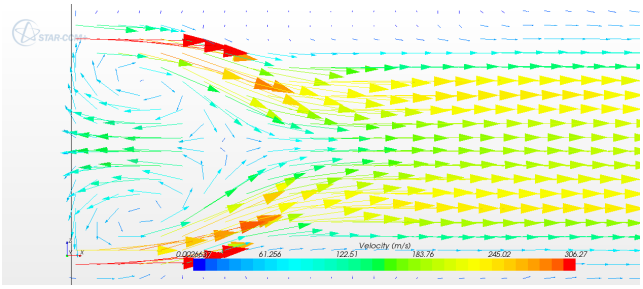

(d) The vortex that forms close to the nozzle inlet for air flow 15 liters/min.

Figure 4.1: The velocity profile of the air jet for the $k-\omega$ SST model. The length of the vortexes in the streamwise direction is $\sim$2mm.

4.2 Multiphase results

The results from the simulations are extracted 30mm and 50mm from the spray nozzle. When the simulation had converged the simulation was continued for a 1000 additional time steps. For each time step, particle properties such as axial velocity is extracted for the particle passing 30mm and 50mm downstream of the spray nozzle. Three parameters: particle velocity, particle diameter and spray cone angle, taken from the experimental study,[1], at 30mm and 50mm from the spray nozzle are used to evaluate the simulations. In [1] values are recored at a number of radial distances from the spray center to show the radial profile of the spray. The axial and size distribution are easy to compare as they are physical entities.The cone angle on the other hand is in [1] measured as brightness of pixels in pictures of the spray. To the author's best knowledge there is no way to translate a brightness in a picture to a physical entity such as volume fraction. The measured spray cone angle is also difficult to accurately attain from the report. The spray cone angles measured in [1] are therefor not used as precise values rather an indication if the results are reasonable or not. In the simulations the normalized volume fraction is used to calculate the spray cone angle. The spray is considered to end at the radial distance measured from the spray center, where the volume fraction is 5% of the maximum value. For the axial velocity and drop size distribution the mass mean values are used.

4.2.1 Parameter study

4.2.1.1 Number of injectors

The number of drop injectors has a major effect on the results. With few injectors the particle velocities are significantly overestimated compared with the values recorded in [1]. When the number of injectors are 17 or 25 the particle velocity matched the recorded velocities good. For example the velocity profile for air flow 15 liters/min and AdBlue flow 0.458g/s is shown in figure 4.2 with 9, 17 and 25 injectors. As can be seen, the case with 17 and 25 injectors match the experimental results better than the case with 9 injectors. The cases with 17 and 25 injectors gives very similar values. This implies that the velocity of the particles will not change singnificantly if the number of injectors are increased further. The same trend as in figure 4.2 is also seen for the other air and AdBlue injection rates.

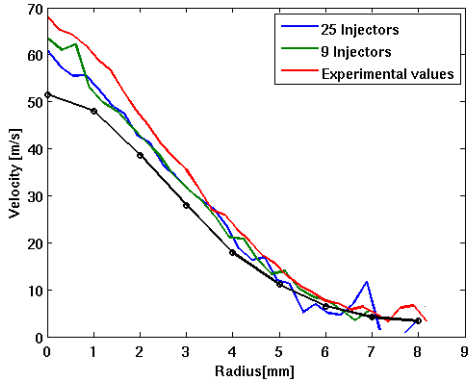

(a) Axial velocity of the drops 30 mm from the spray nozzle.

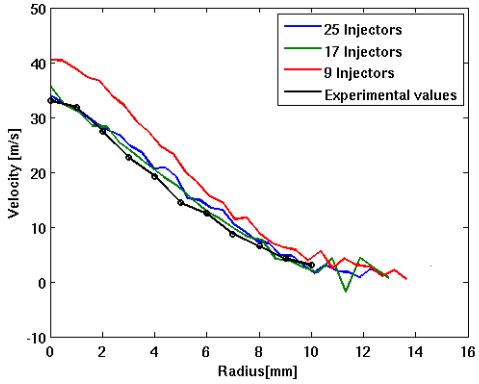

(b) Axial velocity of the drops 50 mm from the spray nozzle.

Figure 4.2: Axial velocity of the particles for air and AdBlue flow 15 liters/min and 0.458g/s respectively. In the simulation the main grid and the $k-\omega$ SST turbulence model is used.

4.2.1.2 Placement of injectors

The first five cases in table 3.8 are concerned with the position of the injectors. If the injectors are placed at the AdBlue injection orifice, case 1, all particles do not escape the vortex directly after the spray nozzle, see figure 4.1. Some particles collide with the spray nozzle and escape the domain because of the escape boundary condition. The remaining particles are spread out through the domain. If the injection surface is chosen to be 2.4mm in diameter, case 4, some of the particles are placed at the outskirts of the air jet. These particles escape the jet and are spread throughout the domain. If the injection surface is placed 3mm downstream of the spray nozzle with a diameter of 1mm the spray cone angle is, compared to measurements [1], too small.

When the injection surface has a diameter of 1.4-2mm there are no profound difference between the cases in drop velocity and size distribution. There is only a slight difference in the spray cone angle, which is marginally larger for the larger injection surface, but as seen in figure 4.3 the difference is insignificant.

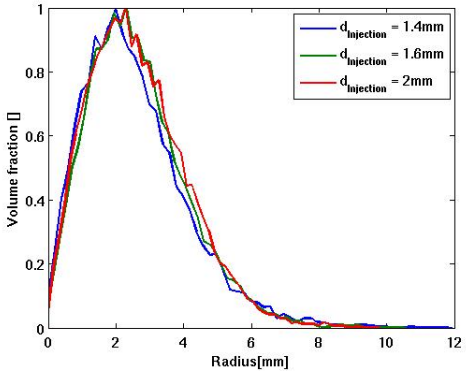

(a) Normalized volume fraction 30 mm from the spray nozzle.

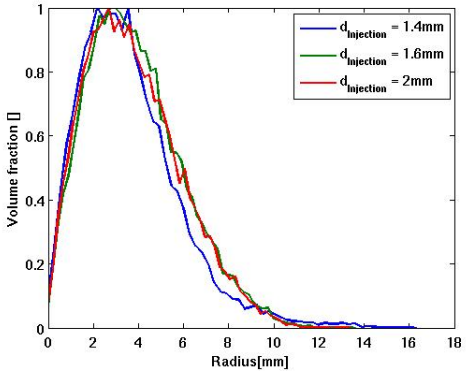

(b) Normalized volume fraction 50 mm from the spray nozzle.

Figure 4.3: Normalized volume fraction for air injection rate of 15 liters/min air and AdBlue 1.46 g/s. In the simulation the main grid and the $k-\omega$ SST turbulence model is used.

4.2.1.3 Particle forces and interactions

The results from simulations with different particle forces and collisions, case 6 to 9 in table 3.8, are shown in table 4.3. The Saffman lift force is seen not to affect the results significantly. There is no significant difference observed between the TAB distortion drag law and the detailed drag law. The inclusion of collisions in the simulation affects the results but slightly, the largest deviation is 4 $\%$ from the base case. The difference is the shape of the

drop size distribution, since the aberration is small and the computational cost of including collisions is large the collisions are neglected.

Table 4.3: The deviations in case 6 to 9 from the base case. In the table, the heading Result is referring to the one result variable of axial velocity, size distribution or spray cone angel that deviate the most from the base case.

Case	Particle forces	Result	Deviation %
Base case	Detailed drag law, buoyancy force, turbulent dispersion	-	-
Case 6	Base case + Saffman lift force	Spray cone angle	2
Case 7	Base case + particle collisions	Size distribution	4
Case 8	TAB drag law, buoyancy force, turbulent dispersion	Spray cone angle	1
Case 9	Spherical drag force, buoyancy force, turbulent dispersion	Axial velocity	25

The assumption that the particles are spherical is not justified by the results. The particles are much faster 50mm from the spray nozzle if assumed spherical than the deformed particle velocity and the validation data. The differences in velocity profiles are shown in figure 4.4

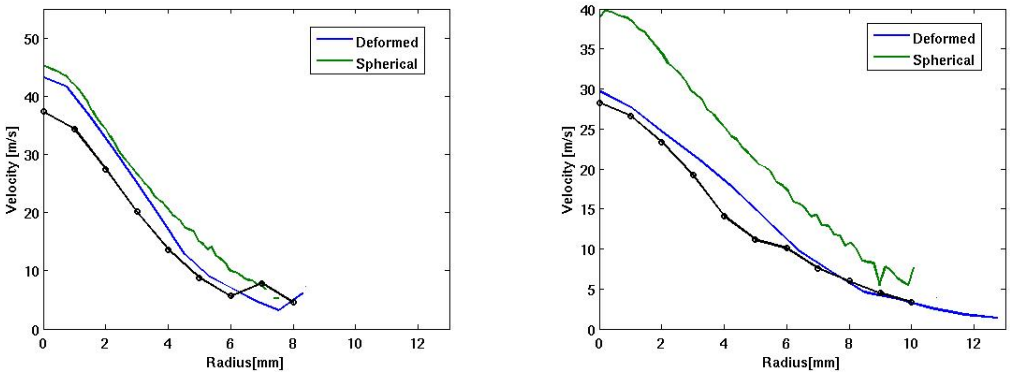

(a) Axial velocity of the particles 30 mm from the spray nozzle. **(b)** Axial velocity of the particles 50 mm from the spray nozzle.

Figure 4.4: Axial velocity of the particles for air flow 15 liters/min and AdBlue flow 1.46g/s. In the simulation the main grid and the $k-\omega$ SST turbulence model is used

4.2.2 Multiphase cases

The multiphase cases simulated are listed in table 3.7a and the results of the axial velocity of the particles can be found in section 4.2.2.1, the drop size distribution in section 4.2.2.2 and spray cone angle in 4.2.2.3.

4.2.2.1 Drop axial velocity

Figure 4.5 shows the axial velocity of the drops for the various multiphase cases using the drop size distribution and injection rate from the experimental study [1]. The left hand side of figure 4.5 shows the velocity profile 30mm downstream the spray nozzle and the right hand side shows the axial velocity 50mm downstream the spray nozzle. At 30mm all simulations overestimate the drop axial velocity but the estimate is improved 50mm from the spray nozzle. The velocity profiles reveal some trends for the various models: the turbulence model $k-\omega$ SST gives lower velocities than the Realizable $k-\varepsilon$ turbulence model and using the unstructured grid results in lower velocities than the other grids. The $k-\omega$ SST turbulence model gives $\sim$13% lower maximum velocity than the Realizable $k-\varepsilon$ turbulence model. The $k-\omega$ SST turbulence model generally gives a lower axial velocity of the drops for all radii but the differences in the results from the two turbulence models decrease with increasing distance from the spray

center. The unstructured grid gives $\sim 5\%$ lower velocity than the main and control grid. The difference between the control and main grid is below 2% and is excluded from the figures for clarity.

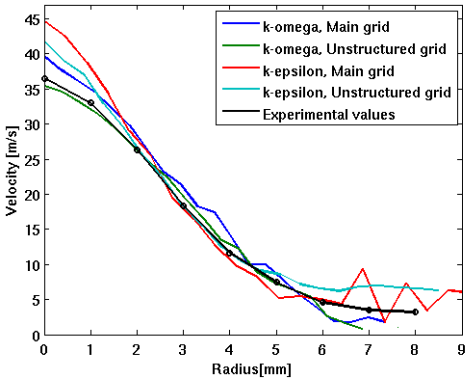

(a) Axial velocity of the drops 30mm from the spray nozzle for air flow 10liter/min and AdBlue flow 0.46g/s.

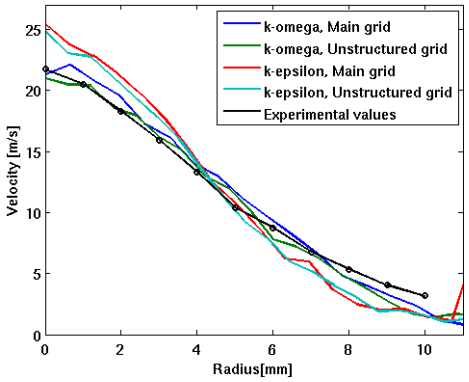

(b) Axial velocity of the drops 50mm from the spray nozzle for air flow 10liter/min and AdBlue flow 0.46g/s.

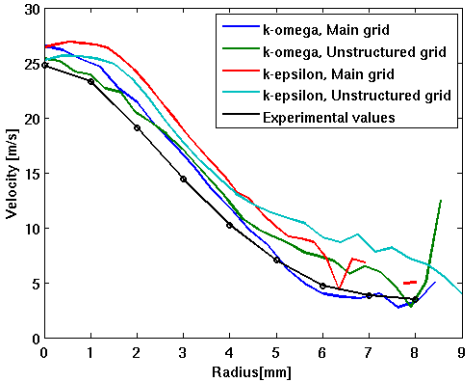

(c) Axial velocity of the drops 30mm from the spray nozzle for air flow 10liter/min and AdBlue flow 1.37g/s.

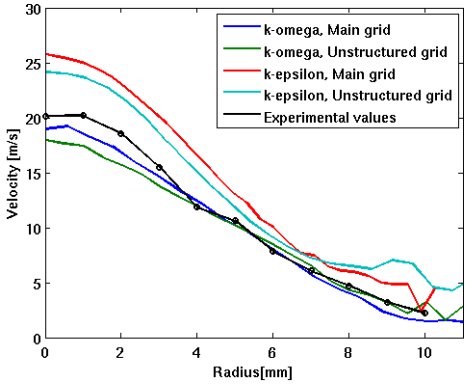

(d) Axial velocity of the drops 50mm from the spray nozzle for air flow 10liter/min and AdBlue flow 1.37g/s.

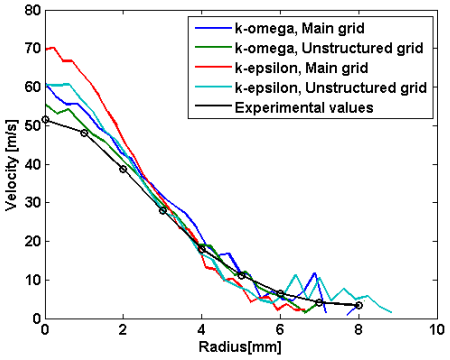

(e) Axial velocity of the drops 30mm from the spray nozzle for air flow 15liter/min and AdBlue flow 0.46g/s.

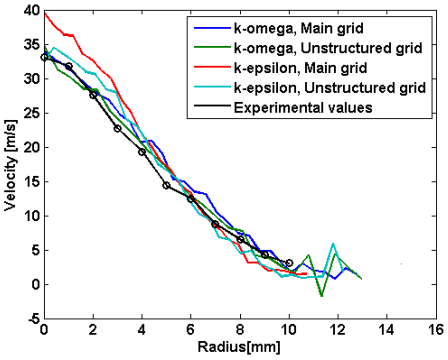

(f) Axial velocity of the drops 50mm from the spray nozzle for air flow 15liter/min and AdBlue flow 0.46g/s.

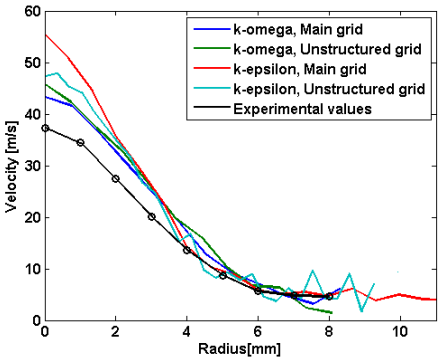

(a) Axial velocity of the drops 30mm from the spray nozzle for air flow 15liter/min and AdBlue flow 1.37g/s.

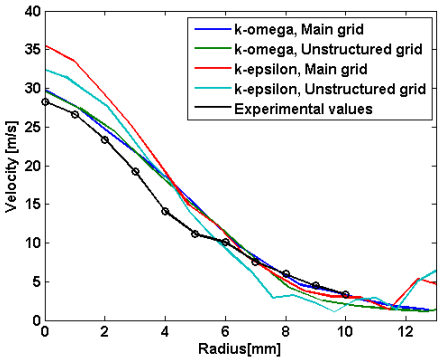

(b) Axial velocity of the drops 50mm from the spray nozzle for air flow 15liter/min and AdBlue flow 1.37g/s.

Figure 4.5: Axial velocity of the drops 30mm and 50mm downstream of the spray nozzle on the left and right hand side in the figure respectively. In these simulations the AdBlue flow and size distribution from [1] is used.

4.2.2.2 Drop size distribution

The drop size distribution for the various simulations is shown in figure 4.6. For high spray radii the size profile is jagged. This is likely a consequence of relatively few particles in the outer edges of the spray and the individual values of the particles become very influential. If the simulations are run with more time steps the size distribution curve is likely to be smoother. No trends between the turbulence models or the computational grids are observed. The simulations slightly underestimate the drop sizes. In figure 4.6a the simulations appear to overestimate the drop diameter but the drop mass mean diameter is smaller than the experimental results because most drops pass close to the center of the spray. No distinct drop size variation is observed across the radius for the results from the simulations or the experimental values, rather leveled size distribution curves are seen. The results from the simulations using the control grid shows very similar values and are omitted from the figures to enhance clarity.

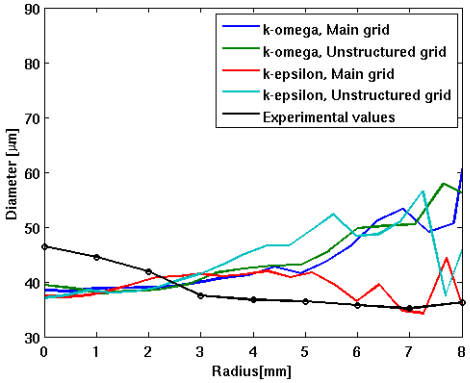

(a) Diameter of the drops 30mm from the spray nozzle for air flow 10liters/min and AdBlue flow 0.46g/s.

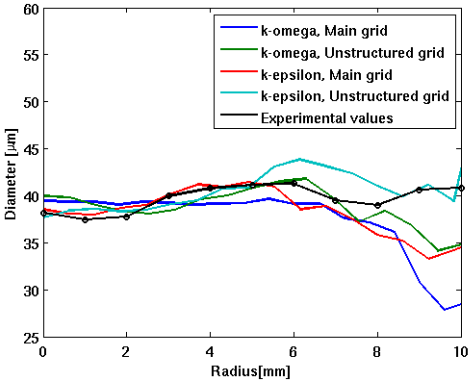

(b) Diameter of the drops 50mm from the spray nozzle for air flow 10liters/min and AdBlue flow 0.46g/s.

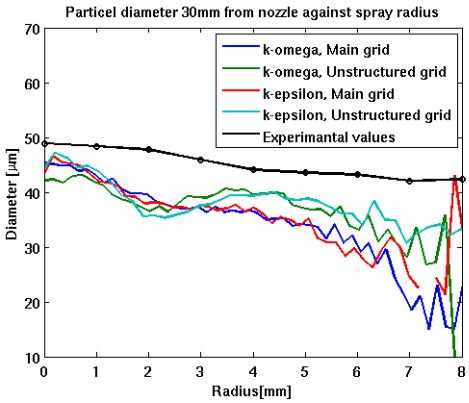

(c) Diameter of the drops 30mm from the spray nozzle for air flow 10liters/min and AdBlue flow 1.37g/s.

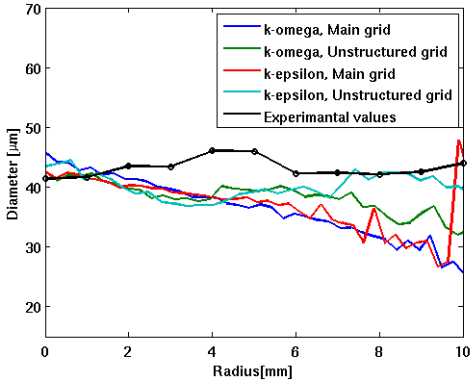

(d) Diameter of the drops 50mm from the spray nozzle for air flow 10liters/min and AdBlue flow 1.37g/s.

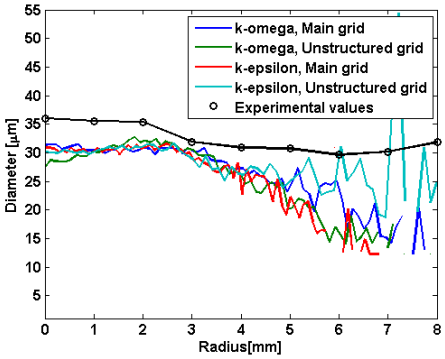

(e) Diameter of the drops 30mm from the spray nozzle for air flow 15liters/min and AdBlue flow 0.46g/s.

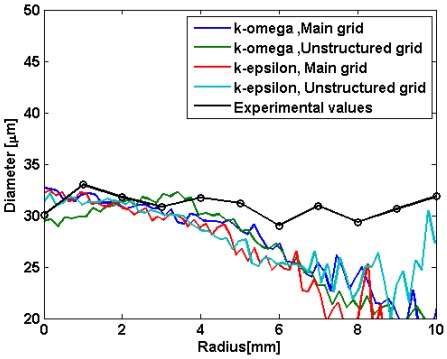

(f) Diameter of the drops 50mm from the spray nozzle for air flow 15liters/min and AdBlue flow 0.46g/s.

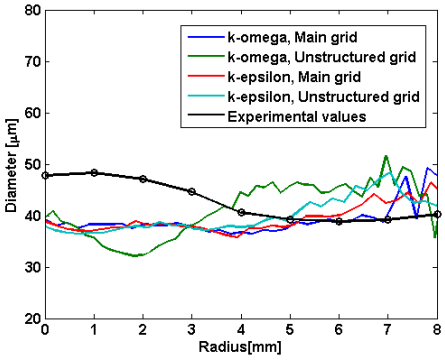

(g) Diameter of the drops 30mm from the spray nozzle for air flow 15liters/min and AdBlue flow 1.37g/s.

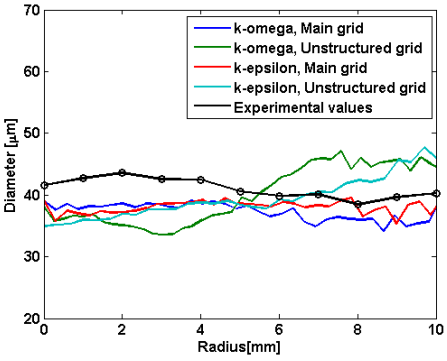

(h) Diameter of the drops 50mm from the spray nozzle for air flow 15liter/min and AdBlue flow 1.37g/s.

Figure 4.6: Diameter of drops 30mm and 50mm downstream of the spray nozzle on the left and right hand side of the figure respectively. The AdBlue flow and size distribution from [1] is used in the simulations.

4.2.2.3 Spray cone angle

The radial distance where the volume fraction is 5% of the maximum is chosen as the end of the spray. Typical volume fraction distributions are shown in figure 4.7. The volume fraction profiles of the other cases have very similar shapes. The main difference between the various cases is the radial distance from the spray center where the volume fraction is 5% of the maximum value. Simulations with the turbulence model $k-\omega$ SST shows a marginally larger spray cone angle than the Realizable $k-\varepsilon$ turbulence model. The spray cone angles are also

slightly larger with the unstructured grid compared to the structured main and control grid. The radial distances are used to calculate the corresponding cone angles, the results are presented in table 4.4.

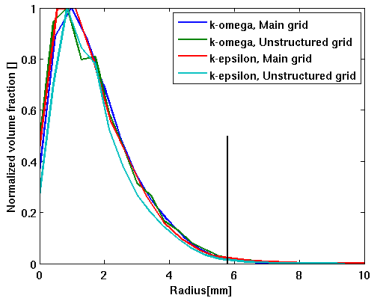

(a) The normalized volume fraction 30mm from the spray nozzle.

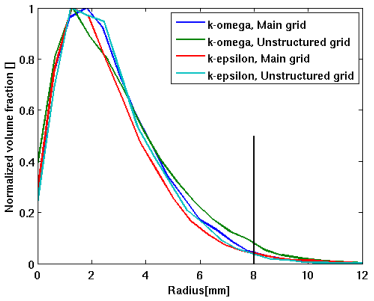

(b) The normalized volume fraction 50mm from the spray nozzle.

Figure 4.7: The normalized volume fractions for air and AdBlue flow 10 liters/min and 0.46g/s respectively. The vertical line marks the spray angle reported in [1].

Table 4.4: The spray cone angles from the simulations and the experimental values [1]. The deviation between the two turbulence models and three grids are minor hence only a mean is presented as the simulation results.

Air flow [Liters/min]	AdBlue flow [g/s]	Simulation 30mm	Simulation 50mm	Experiment 30mm	Experiment 50mm
10	0.46	19.7^o	23^o	18.1^o	19^o
10	1.37	21.1^o	25^o	19.3^o	20^o
15	0.46	17.4^o	21^o	17.1^o	18^o
15	1.37	23.7^o	27^o	18.0^o	20^o

4.3 Breakup results

4.3.1 Jet breakup

The results from equation (3.18) and (3.19), i.e. liquid jet length and the Sauter mean diameter from the jet breakup are shown in table 4.5. These values should be interpreted as indications rather than definite values for the sprays in the thesis. The Sauter mean diameter from the spray manufacturer are given in table 4.5 to enable comparison.

Table 4.5: Approximate values for liquid jet length and Sauter mean diameter, d_{32}, of the spray breakup process. The Sauter mean diameter from the experiments conducted by the spray manufacturer 50mm downstream of the spray nozzle are provided to enable comparison

Air flow [Liters/min]	AdBlue flow [g/s]	Jet length [mm]	d_{32}, equation (3.19) [μm]	d_{32}, Spray manufacturer [μm]
10	0.5	0.57	20	17
10	1.5	1.7	20	27
15	0.5	0.38	12	11
15	1.5	1.1	12	15

The sauter mean diameters from equation (3.19) and the experimental values are relatively close except when the air flow is 10liters/min and the AdBlue injection rate is 1.5g/s.

4.3.2 Drop breakup

The results from the equation (3.20), i.e. the distance during which turbulent breakup can occur, are presented in table 4.6. This distance is an estimate and the values are indications of how far into the system the turbulent breakup occurs.

Table 4.6: Approximate values of how far into the system the turbulent breakup of particles occurs.

Air flow [Liters/min]	AdBlue flow [g/s]	x_{crit} [mm]
10	0.5	0.15
10	1.5	0.25
15	0.5	0.15
15	1.5	0.2

The particle axial velocity for the simulations using the injector manufacturers AdBlue injection rate and size distribution both with and without drop breakup is displayed in figure 4.8. The effect of including drop breakup in the simulations are mainly seen at the higher AdBlue injection rate, i.e in sub-figures 4.8c, 4.8d, 4.8g and 4.8h.

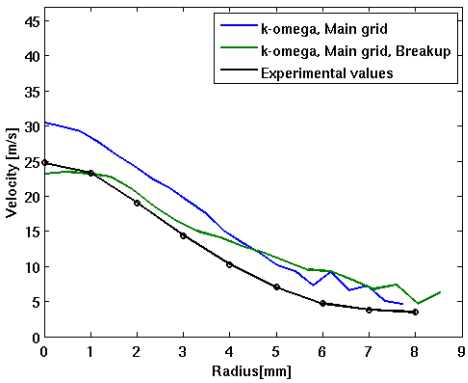

(a) Axial velocity of the drops 30mm from the spray nozzle for air flow 10liters/min and AdBlue flow 0.5g/s.

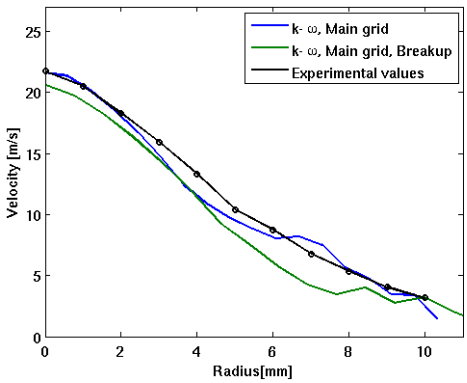

(b) Axial velocity of the drops 50mm from the spray nozzle for air flow 10liters/min and AdBlue flow 0.5g/s.

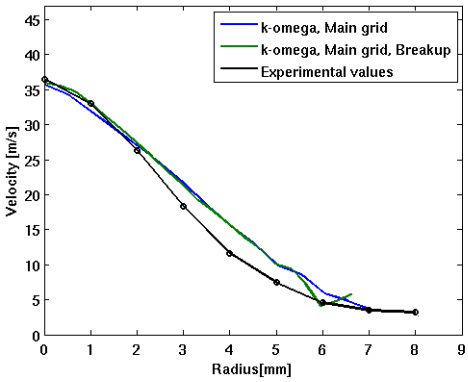

(c) Axial velocity of the drops 30mm from the spray nozzle for air flow 10liters/min and AdBlue flow 1.5g/s.

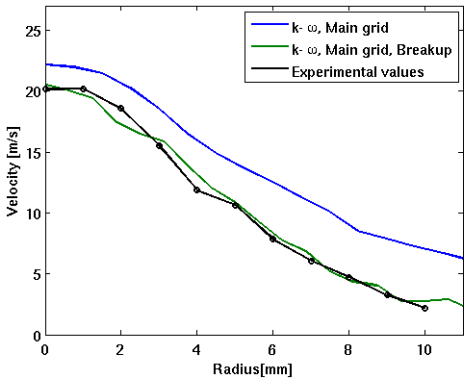

(d) Axial velocity of the drops 50mm from the spray nozzle for air flow 10liters/min and AdBlue flow 1.5g/s.

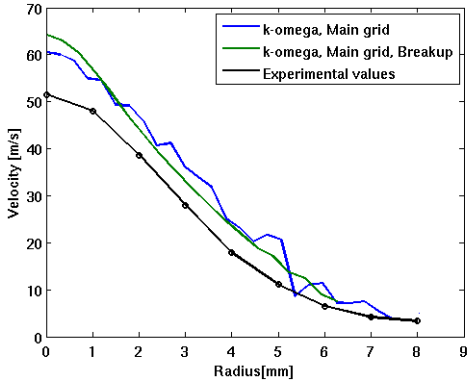

(e) Axial velocity of the drops 30mm from the spray nozzle for air flow 15liters/min and AdBlue flow 0.5g/s.

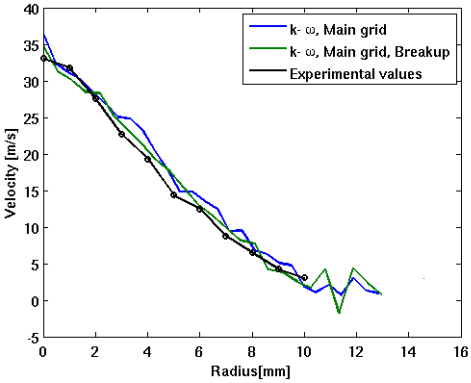

(f) Axial velocity of the drops 50mm from the spray nozzle for air flow 15liters/min and AdBlue flow 0.5g/s.

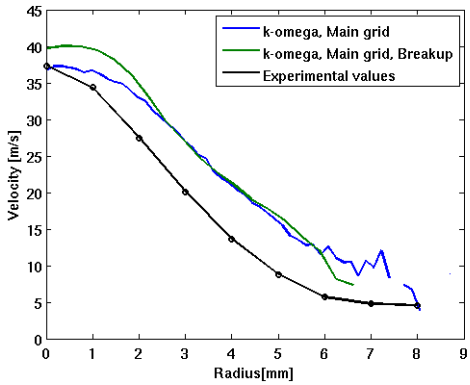

(g) Axial velocity of the drops 30mm from the spray nozzle for air flow 15liters/min and AdBlue flow 1.5g/s.

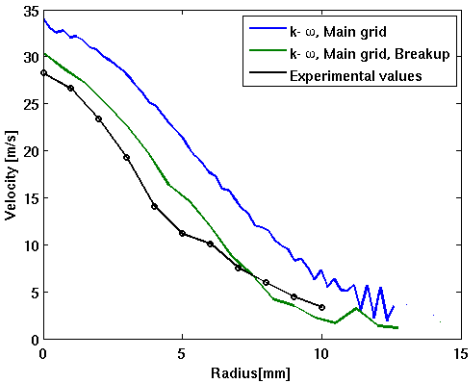

(h) Axial velocity of the drops 50mm from the spray nozzle for air flow 15liters/min and AdBlue flow 1.5g/s.

Figure 4.8: Axial velocity of the drops 30mm and 50mm downstream of the spray nozzle on the left and right hand side of the figure respectively. In the simulations the AdBlue flows and size distributions from the injector manufacturer are used. The turbulence model and computational grid used in the simulations are the $k-\omega$ SST model and main grid.

The mass mean diameter from the simulations with drop breakup acitvated are shown in table 4.7, the mass mean diameters are shown at 10, 15, 20, 25, 30 and 50mm from the spray nozzle together with the initial mass mean diameter. The mean diameter sizes in table 4.7 shows that the drop sizes decrease the first 10mm but then remains virtually constant from 10mm to 50mm from the spray nozzle.

Table 4.7: The development of the mean diameter, in μm, when breakup is included in the simulations.

Air flow [Liters/min]	AdBlue flow [g/s]	Initial	10mm	15mm	20mm	25mm	30mm	50mm
10	0.5	40	34.4	34.4	34.3	34.3	34.3	34.2
10	1.5	114	72	72	72	72	71.9	71.9
15	0.5	28	20.8	20.8	20.8	20.7	20.7	20.8
15	1.5	64	36.7	36.7	36.7	36.7	36.7	36.8

There are no significant differences between the spray cone angle using the spray manufacturer drop size and

AdBlue injection rate compared to the values from the experimental study [1] shown in table 4.4.

5 Discussion

There is no validation data for the single phase simulations. The trend that the $k-\omega$ SST model engenders lower velocities than the Realizable $k-\varepsilon$ does, however, match the theory about different turbulence models [6]. The difference is probably because the $k-\omega$ SST turbulence model is better at predicting the transition between the high velocity, high turbulent gas jet and the low velocity, low turbulent surrounding air.

Number of injectors

Figure 4.2 shows the difference between using low and high numbers of injection points for the drops. A lower number of injection points results in a higher particle velocity. The drops are initially accelerated by the flow but $\sim$15mm downstream of the spray nozzle the drops have reached their maximum velocity. At this point and downstream the particle velocity is higher than the air velocity due to the inertia of the particles. This means that after $\sim$15mm the drops are decelerated by the air flow and the air is accelerated by the drops. The number of injectors needed for the particle velocity to stabilize is found to be $\sim$ 17-25. When a low number of injectors are used the velocity profile at the drop injection becomes very jagged. The velocity of the air very close to the particles is low but the velocity of the air between the particle injection points are high. As the particles are accelerated and move in the radial direction, the high speed air accelerate the particles. This results in a slower and longer acceleration phase for the particles than if more injectors are used. This means that the particles injected by a few injectors have less time to decelerate until they reach the measuring position at 30mm and 50mm from the spray nozzle resulting in a to high velocity.

Injector placement

The injector placement does not affect the results significantly if the particles are injected behind the vortex and with a injection surface diameter in the range of 1.4-2mm. If the particles are injected at the AdBlue injection orifice some drops do not escape the vortex. In reality the AdBlue is injected as a liquid jet rather than drops. Some distance and energy is required to breakup the liquid jet which can explain why the drops in reality do not follow the vortex backwards. When the AdBlue is injected as a liquid jet the entire air flow pattern close to the spray nozzle is different than if the AdBlue is injected as drops. A vortex is expected close to the nozzle as the air is likely to circulate close to the air inlet. However, the vortex cannot have the shape as in the simulations because a liquid jet is present in the vortex center.

Particel-fluid and particle-particle interactions

Neither collision, the Saffman lift force nor the TAB distortion drag law has any pronounced effect on the results compared to the base case including the drag force with deformation, buoyancy force and turbulent dispersion. The effect of deformed drops has a distinct effect on the results. The deformation of drops is therefore important to include as shown in figure 4.4. When the assumption of spherical drops is made the velocity is overestimated at 30mm and even more prominently at 50mm downstream of the spray nozzle. The overestimation of the particle axial velocity is due to the reduction in drag force. The spherical particles are accelerated slower and a longer distance than the deformed particles. After the particles have reached their maximum velocity the spherical particles also decelerate slower than the deformed drops. The velocity difference between the spherical and deformed drops will decrease with increasing distance from the spray nozzle as the relative velocity between the phases decrease. The deformed drops will approach velocity equilibrium with the continuous flow more rapidly when deformation is of importance.

Close to the drop injection the particle Reynolds numbers are above the limit for the drag force coefficient presented in equation 3.15. The particle Reynolds numbers for the mean sized drops are within the allowed range only after a few millimeters, and all particles are within the allowed range $\sim$10mm downstream of the spray nozzle. The drag force coefficient is therefore suitable for the simulations. The rapid reduction of particle Reynolds numbers justifies the assumption that the effect of internal circulation on the drag force is negligible for the large drops.

The effect of evaporation on the drag force is not considered in this thesis due to the low temperature of the system. The temperatures in simulations of the exhaust gas after treatment systems are usually much higher, hence evaporation may have an evident effect on the drag force. The drag force coefficient in 3.15 takes the evaporation into account if the term $(1 + B_T)^{-0.2}$ is multiplied to the equation, where B_T is the heat transfer number [3]. In addition, evaporation will reduce the amount of water i the AdBlue drops. When all the water has evaporated, the drag force should be that of a solid sphere.

Evaporation of the drops results in reduced particle sizes. When the drops are a few micrometer in diameter the Brownian force becomes influential. Micron drops will evaporate completely in a high temperature environment in a short time because of the high surface area to volume ratio. Therefore the Brownian force may still be neglected without affecting the results significantly.

Axial particle velocity

The axial particle velocities for the AdBlue injection rate and drop size from [1] shown in figure 4.5 reveal that there are differences between the two turbulence models and the grids. The results from the two structured grids, the control and main grid, only deviate slightly. The results from the structured and unstructured girds show that the unstructured grid generally gives lower drop axial velocities. A reason could be that the cell length in the stream-wise direction is longer for the structured grids. The velocity gradients close to the spray nozzle and in the vortex are high in the stream-wise direction, the longer cell length in the stream-wise direction of the structured cells could therefore affect the results negatively. The Courant number is in contrast lower for the structured grids. Therefore, it is difficult to deduce which of the grids is the most accurate. The difference does, however, not affect the results considerably.

The difference between the results from the two turbulence models are more significant than the difference between the grids. The $k - \omega$ SST turbulence model matches the experimental results better than the Realizable $k - \varepsilon$. The theory about the turbulence models, section 2.1.1, predicts that the $k - \omega$ SST preforms better for simulations of axisymetric jets is confirmed by the results. The results for the $k - \omega$ SST turbulence model matches the experimental values 50mm from the spray nozzle well. At 30mm from the spray nozzle the particle velocities do not match the experimental values as well because the drops have not yet been sufficiently decelerated by the flow. The errors of the simulations decrease between 30mm and 50mm indicating that the error will continue to decrease with increasing distance from the spray nozzle.

Drop size distribution

The drop size distribution curves shown in figure 4.6, are leveled for all simulation cases and no difference is seen between the turbulence models or computational grids. In all simulations the drop sizes are smaller than the experimental values. A reason could be that $\sim 3\%$ of the drops volume have evaporated at 50mm downstream from the nozzle. One way to improve the drop sizes prediction could be to increase the injected drops sizes to account for the evaporation. The evaporation rate of the particles are increased with increasing temperature. The underestimation is likely to be more obvious in a real exhaust gas after treatment system.

Spray cone angle

The spray cone angles are difficult to evaluate due to the nature of the values reported in [1]. There are no significant differences between the computational grids or turbulence models. The experimental and simulated spray cone angles match reasonably, especially 50mm from the spray nozzle, which indicates that the simulations give realistic values.

Jet breakup

The calculated jet lengths in table 4.5 indicate that the jet lengths are very short for all cases, but the low AdBlue injection cases are shorter than the high. This indicates that in the low AdBlue injection rate cases a recirculation zone are present downstream of the liquid jet curtailing the jet. The calculated Sauter mean diameters for the primary breakup in table 4.5 match the experimental values measured 50mm downstream of the spray nozzle, except for injection rate 10liters/min air and 1.5g/s AdBlue. A plausible explanation for the poor fit for the 10liters/min air and 1.5g/s AdBlue case is that one of the assumptions was fairly constant air velocity over the jet breakup. In the experiments used to develop the equation 3.19 the width of the air jet and, consequently the air flow was much larger

than in the cases in this thesis. The case in this thesis when the air is injected 10liters/min and the AdBlue is injected 1.5g/s the velocity of the air jet decreases the most. The lower velocity at the end of the liquid jet could explain why the calculated mean Sauter diameter is smaller than the measured.

Drop breakup

Figure 4.8 shows the velocity profile for the simulations with the AdBlue injection rate and size distribution from the spray manufacturer with and without drop breakup. The largest difference between the experimental and simulated values are the cases with the higher AdBlue injection rate. These cases also have the largest differences in drop size distribution between the spray manufacturer and [1]. Figure 4.8 shows that the drop size velocity for the high AdBlue injection rate is considerably higher than the experimental values when drop breakup is excluded. The overestimation of the velocity is most likely due to the larger inertia of the larger drops. The larger inertia of the drops means that the drop reacts slower to the movment of the continuous flow, i.e. the Stokes number is larger. The larger inertia causes the drops to accelerate and decelerate slower than smaller drops. Therefore the larger drops have not decelerated as much as the smaller drops 50mm from the spray nozzle. When the drop breakup is included the drop size decreases and consequently the velocity profile matches the experimental values better. The larger drops were most likely present in [1] but not measured. Since no validation data exists for the simulations including the larger drops the accuracy of the results are difficult to asses. The simulations with the smaller drop sizes accurately describe the velocity 50mm from the spray nozzle hinting that the velocities with the larger drops could be realistic.

The drop sizes in table 4.7 show that the drop breakup occurs a short distance from the spray nozzle. The estimated distance from the spray nozzle during which turbulent breakup is important, given in table 4.6, shows that turbulent breakup will only be important a short distance from the spray nozzle. For the largest particle in the system, d_p =350μm, to have a Weber number above the critical Weber number, We_{crit} =11, the relative velocity has to be 46m/s. Relative velocities in the magnitude of 46m/s are only present very close to the drop injection. In reality the liquid jet is accelerated by the air jet, the waves and ligaments formed on the liquid jet surface is accelerated and the ligaments are accelerated before they rupture. This means that the drops created by the liquid jet breakup are not suddenly exposed to high velocity air but rather air of considerably lower velocity than the initial air velocity. This in combination with the diameter generated by the liquid jet breakup indicates that secondary breakup will not be important for the spray. In a simulation of a exhaust gas after treatment system the temperature of the gas will be considerably higher than in the cases simulated in this thesis. A higher gas temperature will heat the drops and as the temperature of the drops increases the surface tension decrease. This causes in turn the particle Weber number to increase and increase the chance of breakup. The acceleration of the drops are however faster than the heating of the drops implying that the relative velocity will decrease faster then the surface tension will decrease, which means that the higher gas temperature is unlikely to cause drop breakup. As the drops evaporate the relative velocity necessary to rupture the drops will increase causing drop breakup far from the spray nozzle to be unlikely.

The simulations without breakup, replicate the measured experimental results well. It is highly unlikely that the drops will experience a relative velocity large enough to rupture the drops, except very close to the spray nozzle. This indicates that drop breakup is not necessary to include in the simulations, rather has a negativity effect on the simulations. The simulations with drop breakup included shows that the drop diameter decrease significantly the first few millimeters creating an incorrect drop size profile. One solution could be to inject a few large drops that shatters to create the correct size distribution. To adjust drop sizes only to include drop breakup seem unnecessary since the simulations without drop breakup are accurate. Injecting larger drops only to be able to include drop breakup in the simulations, is unnecessarily complicated and problematic when drop breakup will not occur except very close to the spray nozzle as relative velocities above 46m/s is needed.

6 Conclusion

6.1 Summary

Two turbulence models, Realizable $k-\varepsilon$ and $k-\omega$ SST, are investigated. The $k-\omega$ SST turbulence model have proven to be superior to the Realizable $k-\varepsilon$ turbulence model in predicting the velocity of the drops. There is no difference in the spray cone angle or drop size distribution between the two turbulence models. The particle forces required to accurately simulate the spray are: the drag force, buoyancy force and forces due to turbulence, presented

in section 3.4.4. The drag force needs to account for the deformation of the drops for the simulation to accurately compute the particle velocity.

The drop injection needs to be downstream of the vortex otherwise some drops will be caught in the vortex, escape the air jet and be spread out in the domain. If the injectors are placed in the radial outskirts of the air jet the particles will also escape the air jet and spread throughout the domain. If the injectors are placed downstream from the vortex, with an injection area diameter of $\sim$1.6mm the spray cone angle will match measured values. A large number of injectors, $\sim$ 25, are needed for the simulations to recreate the drop velocity profile from the experiments.

The liquid jet breakup is due to kinetic energy being transfered from the high velocity co-flowing gas to the liquid jet. The drop size distribution appears to be determined by the liquid jet breakup and drop breakup seems to be of subordinate importance. Drop breakup does not have to be included in the simulations. Including drop breakup will rather decrease the accuracy of the simulations as the drops are ruptured by the high relative velocity the first few millimeters after the drop injection.

6.2 Future work

In the thesis the primary breakup of the spray is not simulated, only characterized. This means that the air and AdBlue flow is unresolved close to the spray nozzle. To understand how the liquid jet disintegrates, simulating the primary atomization is of interest. To simulate the primary atomization will also enable investigations of parameters affecting the spray formation. Literature, for instance reports that addition of swirl to the air jet enhances the liquid jet breakup and spreading of drops [14]. In a resolved simulation of the primary breakup the effect of adding swirl could be investigated.

References

[1] Petter Dahlander and Eugenio de Benito. Urea spray analysis for volvo powertrain, 2010.

[2] Peter Arkins and Loretta Jones. *Chemical Principles - The Quest for Insight*. W. H. Freeman and Company, 3rd edition, 2005.

[3] Henrik Ström, Andreas Lundström, and Bengt Andersson. Choice of urea-spray models in cfd simulations of urea-scr systems. *Chemicla Engineering Journal*, 150(1):69–82, July 2009.

[4] Versteeg. H K and Malalasekera W. *An Introduction to Computational Fluid Dynamics- The finite Volume Method*. Pearson Education, 2nd edition, 2007.

[5] Bengt Andersson, Ronnie Andersson, Love Håkansson, Mikael Mortensen, Rahman Sudiyo, and Berend Van Wachem. *Computational Fluid Dynamics for Engineers*. Cambridge University Press, 8th edition, 2012.

[6] Wilcox David C. *Turbulence Modeling for CFD*. DCW Industries, Inc., 3rd edition, 2006.

[7] Grossmann Christian, Ross Hans-Görg, and Stynes M. *Numerical Time-Dependent Partial Differential Equations for Scientists and Engineers*. Elsevier Inc, 1st edition, 2010.

[8] Wendt John F and Andersson John David. *Computational Fluid Dynamics: an introduction*. Springer, 3rd edition, 2008.

[9] CD-adapco. *Starccm+ User guide*, 7.06.009 edition.

[10] Clayton T. Crowe, John D. Schwarzkopf, Martin Sommerfeld, and Yutaka Tsuji. *Multiphase Flows with Droplets and Particles*. CRC Press Taylor and Francis Group, 2nd edition, 2012.

[11] Roland Clift, John Grace, and Martin E Weber. *Bubbles, Drops and Particles*. Academic Press, INC, 1978.

[12] R. Mei. An approximate expression for the shear lift force on a sperical particle at finite reynolds numbers. *International Journal of Multiphase Flows*, 18(1):145–147, 1992.

[13] S.P. Lin and R.D. Reitz. Drop and spray formation from a liquid jet. *Annual Review of Fluid Mechanics*, 30(1):85–105, 1998.

[14] Lasheras J.C. and Hopfinger E. J. Liquid jet instablility and atomization in a coaxial gas stream. *Annual Review of Fluid Mechanics*, 32(1):275–308, 2000.

[15] Mayer W. O. H and Branam R. Atomization characteristics on the surface of a round liquid jet. *Experiments in Fluids*, 36(4):528–539, 2004.

[16] Marmottant P. and Villermaux E. On spray formation. *Journal of Fluid Mechanics*, 498:73–111, 2004.

[17] Lasheras J.C., Villermaux E., and Hopfinger E. J. Break-up and atomization of a round water jet by a high-speed annular air jet. *Journal of Fluid Mechanics*, 357:351–379, 1998.

[18] Guildenbecher D.R., López-Rivera C., and Sojka P.E. Secondary atomization. *Experiments in Fluids*, 46:371–402, 2009.

[19] Charles Hirsch. *Numerical Computation of internal and External flows: The fundamentals of Computational Fluid Dynamics*. Elsevir Ltd, 2nd edition, 2007.

[20] Kerstin Oom. Personal communication, 2013.

[21] Haynes W.M., editor. *Handbook of Chemistry and Physics*. Taylor and Francis Group, LLC, 93rd edition, 2012-2013.

[22] Sten-Erik Mörtstedt and Gunnar Hellsten. *Data och Diagram - Energi- och kemitekniska tabeller*. Liber, 7th edition, 2008.

[23] Helenbrook B.T. and Edwards C.F. Quasi-steady deformation and drag of uncontaminated liquid drops. *International Journal of Multiphase flow*, 28(10):1631–1657, 2002.

[24] Loth E. Quasi-steady shape and drag of deformable bubbles and drops. *International Journal of Multiphase flow*, 34(6):523–546, 2008.

[25] Omidvar Amir and Khaleghi Hassan. An analytical approach foo calculation of critical weber number of droplet breakup in turbulent gaseous flows. *Arabian Journal for Science and Engineering*, 37(8):2311–2321, 2012.

[26] P.J. O'Rourke and A.A. Amsden. The tab method for numerical calculation of spray droplet breakup. 1987.

[27] Ren B., Zhong W.Q., Jin B.S., and Lu Z.L. Yuan, Y. Modeling of gas-particle turbulent flow in spout-fluid bed by computational fluid dynamics with discrete element method. *Chamical Engineering and Technology*, 34(12):2056–2068, 2011.

[28] Varga C.M., Lasheras J.C., and E.J. Hopfinger. Initial breakup of a small-diameter liquid jet by a high-speed gas stream. *Journal of Fluid Mechanics*, 497:405–434, 2003.